Phase Field Crystal Models for Underdamped Active Systems

Master's Thesis in Physics

Presented by

Dominic Arold

July 15, 2019

Lehrstuhl für Theoretische Physik I
Friedrich-Alexander-Universität Erlangen-Nürnberg

Supervisor: Prof. Dr. Michael Schmiedeberg

Abstract

Active motion is a ubiquitous phenomenon in nature. It can be found across many length scales, from nanoscopic motor proteins traveling along microtubule highways within cells, over microscopic cells themselves actively moving in search for nutrients, up to macroscopic animals. From a physical point of view, the particles in these systems share the ability to steadily convert energy from an internal or external source into mechanical work. Therefore, they force the system out of equilibrium. Any natural organism in equilibrium would be dead. Ensembles of such self-propelled particles, referred to as active matter, show fascinating collective dynamics, like flocking of birds or turbulent-like states in cell colonies.

In many systems, for example bacteria swimming in a viscous fluid, the motion of particles is fully overdamped, meaning that any momentum is immediately dissipated by the environment. A particle's displacement is then effectively given by the forces acting on, and exerted by it. However, Newton's first law states that, in general, massive objects show persistent motion even in the absence of forces, due to their inertia. Like for flying insects or birds, the time scale of inertial motion can become relevant for the dynamics of particles when the friction experienced within their environment is low. Such systems are considered underdamped.

The presented work contributes to the understanding of the collective dynamics of underdamped active matter. Two established coarse-grained continuum models for overdamped systems are extended to explicitly include inertia. Locally averaged fields for particle density, velocity, and direction of self-propulsion describe the dynamics of the resulting models. The original overdamped results are recovered in the low mass limit. In the opposite underdamped regime, it is found that time scales of collective dynamics depend non-trivially on the particle mass. Furthermore, it is shown that introducing inertia into an active system can even lead to additional non-equilibrium states.

Contents

1. Introduction

1.1. Active Matter

Active matter denotes a hole plethora of biological and artificial many body systems composed of self-propelled, interacting particles. For extensive summaries of different topics and models it is reffered to refs. [2–4]. The focus in the following lies first on building up an intuition for the description of single self-propelled particles with the help of a minimal model example. And second, to illustrate how interactions in ensembles of such active particles can be included.

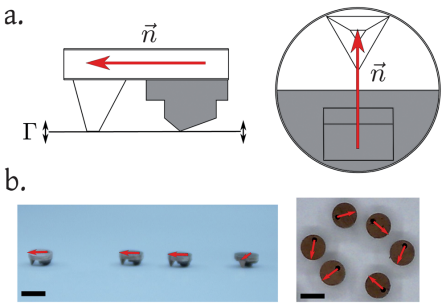

Fig. 1.1.: Polar disks composed of two different materials (gray and white colored) gain energy from a vibrated plate [1]. Due to its asymmetry the disk self-propells along the polar orientation $\vec{n}$.

The term active or self-propelled particles denotes autonomous agents capable of converting energy from an internal or external source into directed motion. Such systems are considered far from equilibrium, since they continually perform work in the form of this motion, which is damped by the environment [5]. A simple generic model for an active system is the active Brownian particle [6]. Its key difference to passive particles is the existence of an intrinsic polar orientation described by a unit vector $\hat{\mathbf{u}}$, along which the particle self-propels by exerting a force f_0 on its environment. An illustrative realization of such polar particles are vibrated polar disks shown in Fig. 1.1. If the friction experienced within the environment is high enough to neglect any inertial effects, the dynamics is referred to as overdamped. With this approximation the Newtonian equations of motion for an active Brownian particle are given by

$$\begin{aligned} \dot{\mathbf{r}} &= v_0\ \hat{\mathbf{u}}(\varphi) + \sqrt{2D}\ \boldsymbol{\Gamma} \\ \dot{\varphi} &= \sqrt{2D_R}\ \xi(t) \end{aligned} \tag{1.1}$$

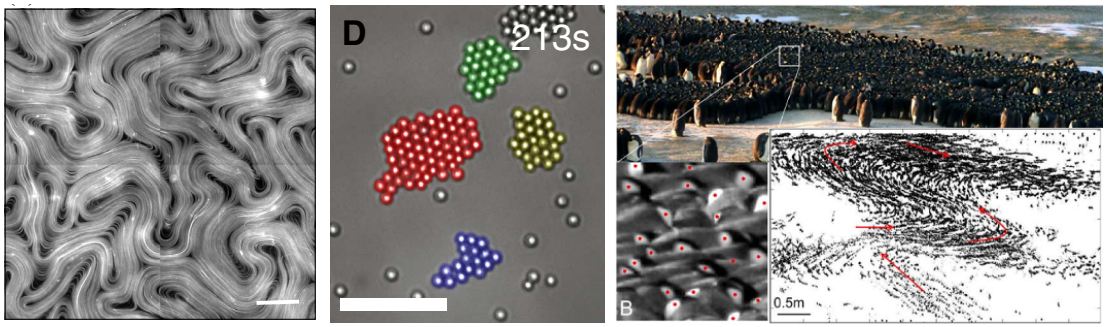

Fig. 1.2.: (left): Long polymer filaments (microtubuls) propelled by motor proteins exibit mesoscale turbulent-like collective dynamics [4, 7]. (middle): Colloids in suspension self-propell via asymmetrical activation under illumination [8]. They assemble in hexagonally ordered clusters, mutually blocking their directions of motion . (right): Collective motion can be observed in pingiun colonies [9]. The red arrows indicate movement directions of different groups.

where φ is the angle of the orientation $\hat{\mathbf{u}} = (\cos(\varphi), \sin(\varphi))^\top$ relative to an fixed axes and $v_0 = f_0/\alpha$ the average self-propulsion velocity in an environment with friction coefficient α. Translational and orientational noise are included with the translational and rotational diffusion coefficients D, D_R and independent δ - correlated white noises ξ and $\mathbf{\Gamma}$, meaning $\langle \xi(t)\xi(t')\rangle = \delta(t-t')$ and analogously for the components of $\mathbf{\Gamma}$. If the activity v_0 is set to zero, Eq. (1.1) is the overdamped Langevin equation for normal Brownian dynamics [10]. It is referred to ref. [6] for details on how the dynamics changes relative to passive Brownian systems when activity is included.
When several active particles interact various collective phenomena can emerge, as illustrated in Fig. 1.2 for some typically considered systems. The minimal active Brownian particle model Eq. (1.1) can be extended to many body systems by including additional terms which account for translational forces and interactions of orientations between particles. In a pioneering work by Vicsek *et al.* such a system is constructed with a local alignment interaction of particle orientations, as explained in Fig. 1.3. Within this model two different states can be observed. For low orientational noise D_R and high enough particle densities a global ordering of particle orientations emerges due to the alignment interaction. This state of collective motion arises without any external orienting fields and makes it therefore a distinct feature of active systems. When rotational noise increases or the average number density decreases local alignment is inhibited resulting in an isotropic state of unordered orientations.

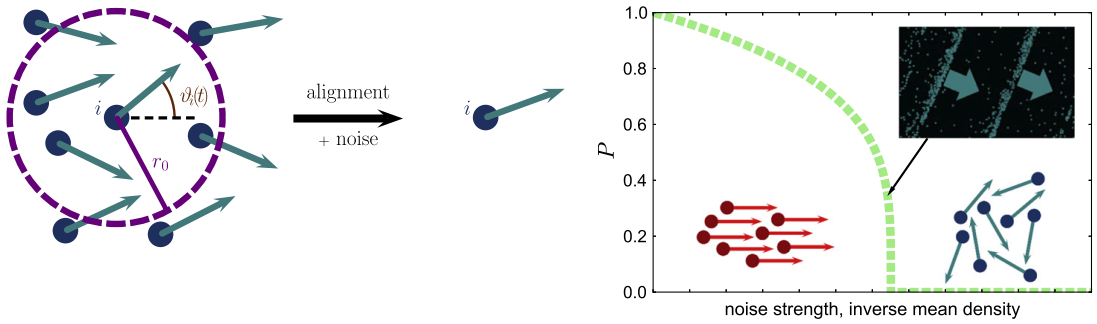

Fig. 1.3.: (left): Sketch of the local alignment interaction in the Vicsek model [5]. In each time step, every particle turns its orientation to the average orientation of neighbouring particles within a given radius r_0. Orientational noise is added and the particles are displaced along their new orientation. (right): State transition in the Vicsek model [5]. P measures the globally averaged polar order of orientations. A value of zero means isotropically distributed orientations (blue particles) and a value one global alignment (red particles). For increasing noise and decreasing density a state transition from globally ordered to isotropically distributed orientations is observed. The inset shows that systems near the transition organize in dense bands of aligned particles. The thick arrows indicate the direction of collective migration.

As the aim of this work is to investigate active systems with inertia the role of the overdamped approximation in the active Brownian particle and the Vicsek model is stressed here explicitly. Both models are formulated in an overdamped limit meaning that the particles' inertia is negligible. Consequently, their motion is given solely by the momentary activity and possible interaction forces with other particles and the environment. This approximation is applicable whenever the friction with the environment is sufficiently high to immediately damp any inertial momentum. Representative examples are microswimmers in a viscous fluid or bacteria binding to an adhesive substrate. However, other active systems, like the macroscopic disks in Fig. 1.1 are known to be influenced by their inertial momentum [11].

1.2. The Phase Field Crystal Model

Pattern formation is a widespread topic in non-equilibrium physics [12]. A commonly used theoretical basis for their description are deterministic non-linear partial differential equations, motivated on a phenomenological basis. One prominent example is the phase field crystal (PFC) model for crystallization phenomena. Essential aspects of this model which are relevant for this work are summarized. A more extensive overview is given in ref. [13].
The PFC model descrivbes a many particle system via an order parameter field $\psi(\mathbf{r})$ which is interpreted as a rescaled one body density. An isotropic state $\psi = const.$ is associated with a fluid phase, while a spatially modulated field captures basic symmetry properties of a crystalline structure. In equilibrium physics, the stability of a thermodynamic phase can be associated with the minimum of a suitable grand canonical free energy functional with respect to the one body density of the system. In analogy to that, Elder *et al.* introduced the PFC model [14, 15] in form of a free energy functional for the order parameter field ψ, which reads

$$\mathcal{F}[\psi] = \int d\mathbf{r}\ \frac{\psi}{2}\left[\epsilon + \left(q_0^2 + \nabla^2\right)^2\right]\psi + \frac{\psi^4}{4}. \tag{1.2}$$

Minima of this functional are given from the temperature like parameter ϵ. For $\epsilon > 0$ a constant fluid phase minimizes the free energy while for positive values the ϵ term can drive an instability of the homogeneous state. The fourth order term is then necessary for the stability of the system as it inhibits divergences of the order parameter field. The second linear term models a preferred periodic modulation in ψ with characteristic length scale $l_0 = 2\pi/q_0$.
The non-equilibrium dynamics of the order parameter field can be formulated via the time evolution

$$\frac{\partial\psi}{\partial t} = \nabla^2\frac{\delta\mathcal{F}}{\delta\psi} = \nabla^2\left[\epsilon + \left(q_0^2 + \nabla^2\right)^2\psi + \psi^3\right] \tag{1.3}$$

which is chosen in form of a continuity equation $\dot{\psi} = -\nabla\cdot\mathbf{j}$ in order to ensure mass conservation. It is noted that replacing the second spatial derivative in front of the functional derivative with a minus sign in Eq. 1.3, results the Swift-Hohenberg equation for pattern formation [17]. Due to the functional derivative in the dynamical equation,

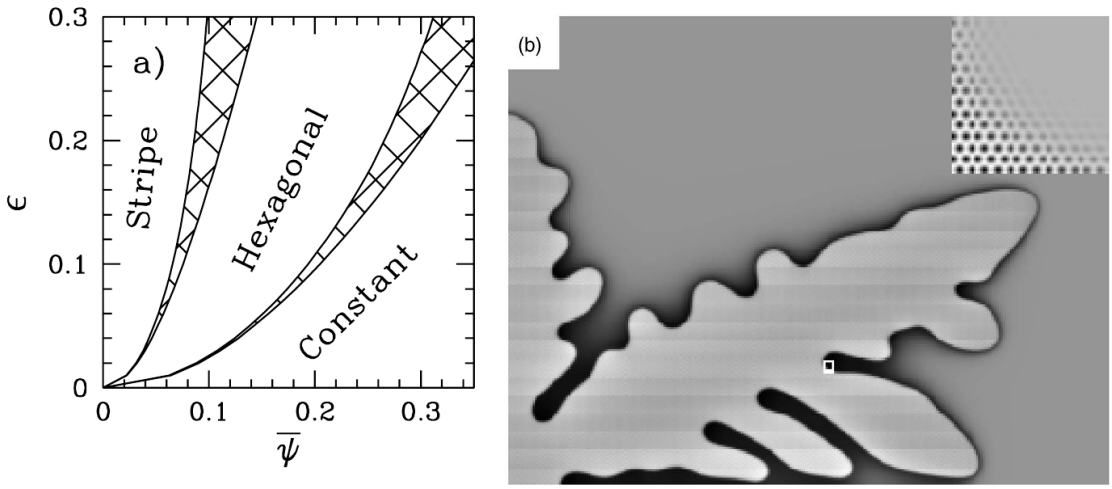

Fig. 1.4.: (a): Phase diagram of the PFC model [14]. The temperature ϵ and mean density $\overline{\psi}$ determine the observed pattern in equilibrium (ϵ is defined here with opposite sign). Constant: liquid phase with homogeneous density. Hexagonal: Spatially modulated density of triangular ordered peaks. Stripe: Spatially modulated density of periodic stripes along one spatial direction. Hatched regions indicate coexistance of neighbouring phases. (b): Crystal growth of a PFC system in the crystallinne phase started from homogeneous initial conditions [16]. Gray scale corresponds to the local concentration of hexagonal peaks in the order parameter field. The boxed region is magnified in the inset, showing the order parameter field at the boundary between hexagonal and liquid phase.

the time evolved order parameter field minimizes the free energy $\mathcal{F}$. Depending on the system parameters different equilibrium phases correspond to this minimum, shown in Fig. 1.4 (a). The basic PFC model is able to capture the essential geometric symmetry properties of an hexagonal crystal phase. Also non-equilibrium phenomena like crystal growth or grain boundaries are naturally included with the time evolution Eq. 1.3. Due to this relatively simple evolution equation, crystallization processes in systems of several 10^7 particles can be efficiently computed on diffusive time scales, as exemplary shown in Fig. 1.4 (b). This is a clear advantage of the PFC approach compared to other methods like direct atomistic simulations or density functional theory (DFT). Direct particle simulations explicitly iterate Newtons equations of motion for the N particle problem and therefore resolve atomistic time scales of the interactions, but are also practically bound to this smaller time regime. DFT and its dynamical extension use the particle interactions to derive observables like particle correlations directly on the level of

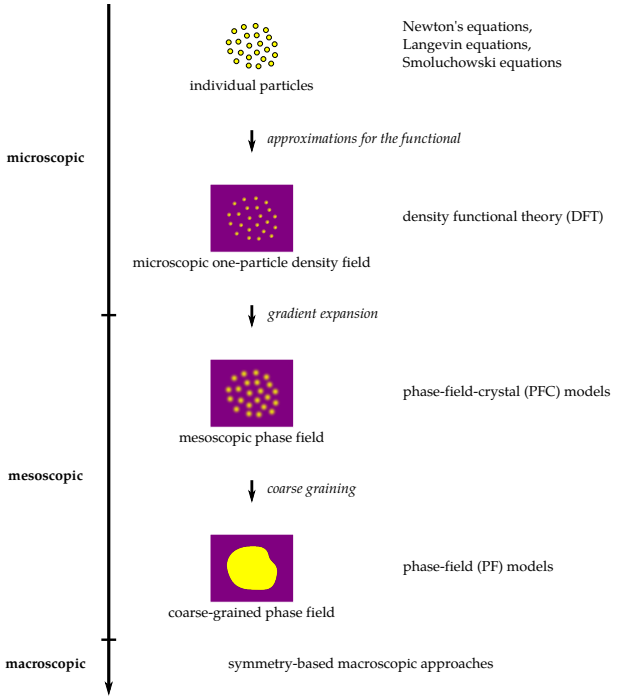

Fig. 1.5.: Coarse-graining of length and time scales across modeling approaches [13]. Explicitly solving the N particle system of (Newton) equations resolves atomistic length and time scales. DFT uses a functional for the one body density field in order to make direct statistical predictions above the atomistic time scale. The PFC model approximates such a functional for an efficient inclusion of basic physical properties in different phases. Restricting to functional terms for the description of phase boundaries results in further coarse-grained phase field models.

diffusive time scales with the help of a free energy functional for the one body density. In this context the PFC functional should be regarded as an approximated DFT, which can also be derived from the latter [18]. Approximated here means that the PFC functional Eq. (1.2) is a expansion of a general functional in powers of ψ plus a gradient expansion (corresponding to an expansion in powers of the wave vector $\mathbf{k}$ in Fourier space, since a derivative in real space transforms to a multiplication in Fourier space $\nabla^{2n} \leftrightarrow (-1)^n k^{2n}$). The PFC model therefore is classified into a hierarchy of different space and time scales of description, as summarized in Fig. 1.5. By using the mean field ψ as rescaled particle density, the PFC model effectively averages out the time scale of atomistic interactions and only resolves the formation of crystalline structures on the diffusive time scale.

1.3. Overdamped Active Crystals

This last introductory part aims to make the reader familiar with the active phase field crystal model, introduced by Menzel *et al.* [19, 20]. Results obtained within this overdamped model are summarized here, as they are needed later on for the discussion of the underdamped generalization of active crystals in Ch. 4.2, when the influence of inertia on this system is investigated.
Like the PFC model, the active crystal model is a coarse-grained continuum description for the mean one body density ψ and aims to characterize crystallization, but with the additional ingredient of activity. Consequantly, since particles now are able to self-propell, a mean orientation field $\mathbf{P}$ is needed to capture local polar order. The dynamical equations for these two fields are motivated and derived from dynamical density functional theory [21] and read

$$\begin{aligned} \frac{\partial \psi}{\partial t} &= \nabla^2 \frac{\delta \mathcal{F}}{\delta \psi} - v_0 \nabla \cdot \mathbf{P} \\ \frac{\partial \mathbf{P}}{\partial t} &= \left(\nabla^2 - D_R\right) \frac{\delta \mathcal{F}}{\delta \mathbf{P}} - v_0 \nabla \psi \end{aligned} \tag{1.4}$$

with the activity parameter v_0 and rotational diffusion D_R. The coupling between the two fields via the gradient terms is a minimalistic approach, which is consistent with symmetry arguments [19]. Like in the PFC model for passive particles the effective interaction forces are given in form of a free energy functional $\mathcal{F} = \mathcal{F}_{PFC} + \mathcal{F}_P$. The two contributions for translational interaction $\mathcal{F}_{\mathrm{PFC}}$ and interaction of orientations $\mathcal{F}_P$ are specified to

$$\begin{aligned} \mathcal{F}_{\mathrm{PFC}} &= \int d\mathbf{r} \; \frac{\psi}{2} \left[\epsilon + \left(1 + \nabla^2\right)^2\right] \psi + \frac{1}{4}\psi^4 \\ \mathcal{F}_P &= \int d\mathbf{r} \; \left[\frac{C_1}{2}\mathbf{P}^2 + \frac{C_4}{4}\left(\mathbf{P}^2\right)^2\right]. \end{aligned} \tag{1.5}$$

When the activity v_0 is set to zero, the dynamical equation for ψ is identical to the PFC model in Eq. (1.3) (the preferred wave number q_0 is set to one here). The additional interaction of orientations $\mathcal{F}_P$ is known from the Toner-Tu theory on flocking [22]. For $C_1, C_4 > 0$ any polar ordering $\mathbf{P} > \mathbf{0}$ which arises from the density gradient term, is suppressed, while for $C_1 < 0, C_4 > 0$ a net orientation can also be observed in the

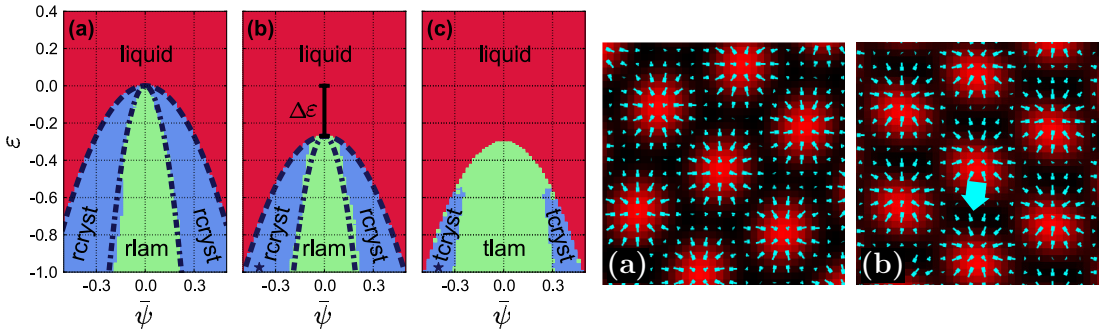

Fig. 1.6.: (left): State diagram for the overdamped active PFC model with liquid state (red), resting/traveling crystal state (blue) and resting/traveling stripe state (green) [19]. For $v_0 = 0$ the original PFC diagram for passive particles retained (a). For non-zero activity the kinetic energy input shifts the state diagram by $\Delta\epsilon$ to lower temperatures. Stable structures remain at rest (b). Above a critical activity $v_{0,c}$ the additional kinetic energy is, instead of melting the crystalline structures further, used for self-propulsion (c). (right): Snapshots of density and orientation field in the (a) resting crystal $v_0 = 0.1$ and (b) traveling crystal state $v_0 = 0.5$, respectively [19]. The blue arrow in (b) indicates the migration direction of the shown density peaks. Fixed parameters read $(\overline{\psi}, \epsilon, C_1, C_4, D_R) = (-0.4, -0.98, 0.2, 0, 0.5)$.

absence of density gradients. It is noted that specifying the interaction terms on the coarse-grained continuum level with Eq. (1.5) is different to specifying them directly in the corresponding Newtonian equations of motion, from which the field equations (1.4) are derived. Employing interaction rules directly in the particle equations gives a clear picture of their physical background. On the other hand, employing their effective interplay in the functionals at the continuum level, is useful to understand large scale collective dynamics in the system.

First, the case $C_1 > 0$, $C_4 = 0$ is considered, meaning that polar order arising from density gradients 'costs' free energy. The determined non-equilibrium phase diagram for varying temperature parameter ϵ and mean density $\overline{\psi}$ is shown in Fig. 1.6. The phase diagram is symmetric under sign change in $\overline{\psi}$ since the dynamical equations (1.4) with the chosen functionals are invariant under the transformation $\psi \to -\psi, \mathbf{P} \to -\mathbf{P}$. For no active drive $v_0 = 0$ the original PFC phase diagram for passive particles is observed. When activity starts to increase the additional input of kinetic energy shifts the phase boundaries to lower temperatures by a value of $\Delta\epsilon \propto v_0^2/C_1$. Activity therefore effectively melts crystals and stripe patterns near the liquid phase boundary. The stable non-liquid density patterns remain at rest. An example of this is shown in Fig. 1.6 where the

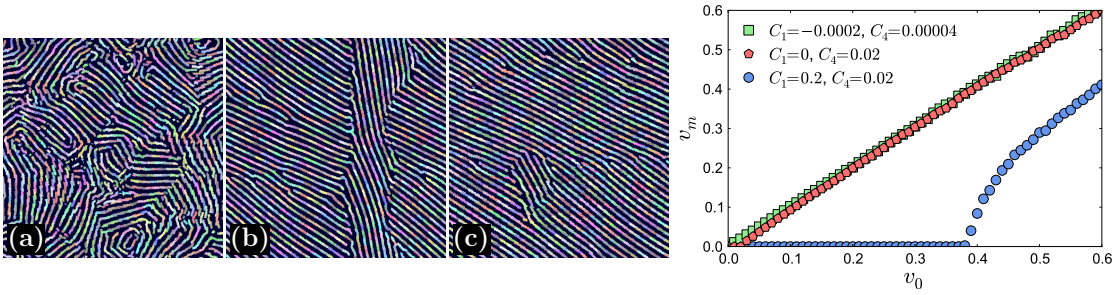

Fig. 1.7.: (left): Coarse-graining of collectively moving density peak clusters in the traveling crystal state over time, (a) $t = 4500$, (b) $t = 50000$, (c) $t = 70000$ [20]. Shown are pieces of peak trajectories. In the long time limit, a global migration direction emerges. (right): Sample averaged crystal velocity v_m in the long time limit [20]. For $C_1 > 0$, the peaks are first at rest and start to collectively migrate above a critical activity $v_{0,c}$. For $C_1 < 0$, collective motion is observed for all activities, due to the favoured polar order. Fixed parameters read $(\overline{\psi}, \epsilon, v_0, C_1, C_4, D_R) = (-0.4, -0.98, 0.5, 0.2, 0, 0.5)$ if not stated otherwise.

orientation field points along the gradient of density peaks. So, activity opposes the accumulation of density in peaks induced by the PFC interaction. This is why lower temperatures are necessary for the formation of non-homogeneous density patterns. When activity is increased above a threshold value $v_{0,c}$, this situation changes. Instead of melting the crystalline structures further, the additional kinetic energy input from activity is transduced into self-propulsion of the density peaks. Consequently the state diagram is no longer shifted to lower temperatures. Self-propulsion spontaneously sets in due to an instability in the order parameter fields [20, 23]. Such a situation is shown in Fig. 1.6, where the density peak positions and defect centers of the orientation field are shifted relative to each other, resulting in a net orientation when averaging the orientation field over a peak area. The peak starts to move due to this asymmetry.

When started from homogeneous initial conditions, the emerging density peaks in the traveling crystal state have no preferred direction of movement. Over time, several clusters of collectively moving peaks form, which start to grow on the cost of others until in the long time limit a global direction of motion emerges, in which the hole crystalline structure migrates collectively. A time series of this formation process is shown in Fig. 1.7. In the final collective motion state, the migration velocity of the traveling crystal is measured with the sample averaged peak displacement velocities $\mathbf{v}_i$ to $v_m = \sum_i \|\mathbf{v}_i\| / N$, where N is the number of peaks in the system. The crystal velocity is shown in Fig. 1.7 in dependence of v_0. For $C_1 > 0$ the peaks are first at rest in

the resting crystal state and start spontaneously to migrate after the transition to the traveling crystal state. There, the final crystal velocity increases with active drive v_0. For $C_1 < 0$ the system favours the polarized state also for lower active drive, leading to collective migration with $v_m = v_0$ for all activities.

2. A Model for Underdamped Active Systems

Much of the current research on active matter concentrates on the description of microscopic systems in which its constituents are in a viscous environment. Typical examples include protein filaments in motility assays [24], cell colonies [25–27], biological or artificial micro swimmers [28–30], all surrounded by a viscous background fluid at low Reynolds numbers or binding to an adhesive substrate. These systems are overdamped, meaning the motion of particles is solely governed by the momentary forces acting on them. However, Newton's first law formulates that massive objects, due to their inertia, resist any change in momentum. While not relevant on the microscopic length scale in solution, inertial effects more probably become relevant in typical macroscopic realizations of active matter, like flocks of birds [31, 32] or artifically made massive robots moving on a two dimensional plate [1, 33, 34]. For the latter the influence of inertia on the long time statistics was observed recently [11].

The theoretical description of active matter produced a wide range of particle based models which explicitly incorporate the microscopic interactions [35–38]. Another approach to model such systems is the formulation of continuum theories which describe systems typically on a length scale above the particle resolution. Such coarse grained models have a potential of unifying concepts of active matter and identify their basic principles. Dynamical density functional theory has proven to be a useful ansatz to derive effective continuum models from microscopic equations of motion [21, 28]. Such models are already able to predict experimental observations of microscopic systems, like bacterial colonies [39], ensembles of microswimmers [29, 40] or active nematics [4, 41, 42].

Following their idea a mean field continuum model for underdamped active systems is derived from underlying microscopic eqautions of motion in the next section. It serves as the ground, on which two systems are specified afterwards.

2.1. Formulation of the Model

The presented derivation in this section follows [43] concerning the calculation steps and coincides with it when active components are neglected. Those additional active terms do not change the principal calculation, but give additional contributions in each step, which are described respectively. The inclusion of activity follows similar derivations for overdamped active systems [21, 30].
The system consists of N identical polar particles of mass m with position and momentum coordinates $\mathbf{r}^N = \{\mathbf{r}_1, \mathbf{r}_2, ..., \mathbf{r}_N\}$ and $\mathbf{p}^N = \{\mathbf{p}_1, \mathbf{p}_2, ..., \mathbf{p}_N\}$. They self-propel with an active force amplitude f_0 into the direction of their orientation given by the unit vectors $\hat{\mathbf{u}}^N = \{\hat{\mathbf{u}}_1, \hat{\mathbf{u}}_2, ..., \hat{\mathbf{u}}_N\}$. The derivation is restricted to effectively two dimensional systems where an angle φ_i determines the orientation $\hat{\mathbf{u}}_i = (\cos(\varphi_i), \sin(\varphi_i))^\top$. The force $\mathbf{F}_i = \mathbf{F}^{(1)}(\mathbf{r}_i) + \mathbf{F}^{(2)}(\mathbf{r}^N)$ incorporates an external potential force $\mathbf{F}^{(1)}(\mathbf{r}_i) = -\nabla_{\mathbf{r}_i} V^{\text{ext}}(\mathbf{r}_i)$ and particle interactions $\mathbf{F}^{(2)}(\mathbf{r}^N) = -\sum_j \nabla_{\mathbf{r}_i} V^{(2)}(\mathbf{r}_i, \mathbf{r}_j)$ with the pair interaction potential $V^{(2)}(\mathbf{r}_i, \mathbf{r}_j)$. Analogously to these translational forces, particles change their orientation due to the torque $G_i(\mathbf{r}^N, \varphi^N) = G^{(1)}(\mathbf{r}_i, \varphi_i) + G^{(2)}(\mathbf{r}^N, \varphi^N)$ with a one particle contribution $G^{(1)}(\mathbf{r}_i, \varphi_i)$ and a pairwise interaction torque $G^{(2)}(\mathbf{r}^N, \varphi^N)$. The corresponding Langevin equations for the underdamped motion of the particle ensemble then reads

$$\begin{aligned} \frac{\mathrm{d}\mathbf{r}_i}{\mathrm{d}t} &= \frac{\mathbf{p}_i}{m} \\ \frac{\mathrm{d}\mathbf{p}_i}{\mathrm{d}t} &= -\gamma\, \mathbf{p}_i + \mathbf{F}_i(\mathbf{r}^N) + f_0\, \hat{\mathbf{u}}_i + \sqrt{2D}\; \mathbf{\Gamma}_i(t) \\ \frac{\mathrm{d}\varphi_i}{\mathrm{d}t} &= G_i(\mathbf{r}^N, \varphi^N) + \sqrt{2D_R}\; \xi_i(t) \end{aligned} \tag{2.1}$$

where $\gamma = \alpha/m$ is the damping constant with the friction α and D, D_R are translational and rotational diffusion constants. $\mathbf{\Gamma}_i(t)$, $\xi_i(t)$ are independent δ - correlated white noises, meaning $\langle \xi_i(t)\, \xi_j(t') \rangle = \delta_{ij}\, \delta(t - t')$ and analogously for the components of $\mathbf{\Gamma}_i$. Note that the damping γ and diffusion D are not necessarily related via the Einstein relation, since they e.g. might describe the interaction with a substrate instead of a thermal bath.
These microscopic equations of motion for the stochastic state variables are converted into the corresponding Fokker-Planck equation of the N body phase space probability density $f^{(N)}(\mathbf{r}^N, \mathbf{p}^N, \hat{\mathbf{u}}^N, t)$ which gives the probability of finding the system in a

configuration $\mathbf{r}^N$, $\mathbf{p}^N$, $\hat{\mathbf{u}}^N$ at time t [10]. The resulting dynamical equation reads

$$\frac{\partial f^{(N)}}{\partial t} = \sum_{i=1}^{N} \Big[-\frac{\mathbf{p}_i}{m} \cdot \nabla_{\mathbf{r}_i} f^{(N)} + \gamma \, \nabla_{\mathbf{p}_i} \cdot \Big(\mathbf{p}_i \, f^{(N)} \Big) - \mathbf{F}_i \cdot \nabla_{\mathbf{p}_i} f^{(N)} - f_0 \, \hat{\mathbf{u}}_i \cdot \nabla_{\mathbf{p}_i} f^{(N)} + D \, \nabla^2_{\mathbf{p}_i} f^{(N)} - \partial_{\varphi_i} \Big(G_i \, f^{(N)} \Big) + D_R \, \partial^2_{\varphi_i} f^{(N)} \Big] \tag{2.2}$$

This N body problem can be simplified by defining the n body reduced phase space distribution functions

$$f^{(n)}(\mathbf{r}^n, \mathbf{p}^n, \varphi^n, t) = \frac{N!}{(N-n)!} \int d\mathbf{r}^{(N-n)} \int d\mathbf{p}^{(N-n)} \int d\varphi^{(N-n)} \; f^{(N)}(\mathbf{r}^N, \mathbf{p}^N, \varphi^N, t) \tag{2.3}$$

where $N-n$ of the N bodies' state variables are integrated out. Equivalently, integrating Eq. (2.2) over $N-1$ sets of particle variables then yields the dynamical equation for the one body distribution

$$\begin{aligned} \frac{\partial f^{(1)}}{\partial t} = & -\frac{\mathbf{p}_1}{m} \cdot \nabla_{\mathbf{r}_1} f^{(1)} + \gamma \, \nabla_{\mathbf{p}_1} \cdot \Big(\mathbf{p}_1 \, f^{(1)} \Big) - \mathbf{F}^{\text{ext}} \cdot \nabla_{\mathbf{p}_1} f^{(1)} \\ & - \int d\mathbf{r}_2 \int d\mathbf{p}_2 \int d\varphi_2 \; \mathbf{F}^{(2)} \cdot \nabla_{\mathbf{p}_1} f^{(2)} - f_0 \, \hat{\mathbf{u}}_1 \cdot \nabla_{\mathbf{p}_1} f^{(1)} + D \, \nabla^2_{\mathbf{p}_1} f^{(1)} \\ & - \partial_{\varphi_1} \Big(G^{(1)} \, f^{(1)} \Big) - \int d\mathbf{r}_2 \int d\mathbf{p}_2 \int d\varphi_2 \; \partial_{\varphi_1} \Big(G^{(2)} \, f^{(2)} \Big) + D_R \, \partial^2_{\varphi_1} f^{(1)} \end{aligned} \tag{2.4}$$

where it is assumed that the N body density and its first derivatives decay to zero for all $\mathbf{r}_i, \mathbf{p}_i \to \infty$ and are periodic in φ_i. The latter assumption is also used for the torques G_1, G_2. The reduced one body phase space density $f^{(1)}(\mathbf{r}_1, \mathbf{p}_1, \varphi_1, t)$ gives the probability of finding a particle at the position $\mathbf{r}_1$ with momentum $\mathbf{p}_1$ and orientation $\hat{\mathbf{u}}_1$ at time t. Note that due to particle interactions Eq. 2.4 still depends on the two body density $f^{(2)}(\mathbf{r}_1, \mathbf{r}_2, \mathbf{p}_1, \mathbf{p}_2, \varphi_1, \varphi_2, t)$.

For the next step, the mean field quantities number density ρ, momentum current $\mathbf{j}$ and orientation current $\rho\mathbf{P}$ with the mean orientation field $\mathbf{P}$ are defined as

$$\begin{aligned}\rho(\mathbf{r}_1,t) &= \int d\mathbf{p}_1 \int d\varphi_1 \; f^{(1)}(\mathbf{r}_1,\mathbf{p}_1,\varphi_1,t)\\ \mathbf{j}(\mathbf{r}_1,t) &= \int d\mathbf{p}_1 \int d\varphi_1 \; \frac{\mathbf{p}_1}{m} \; f^{(1)}(\mathbf{r}_1,\mathbf{p}_1,\varphi_1,t)\\ \rho\,\mathbf{P}(\mathbf{r}_1,t) &= \int d\mathbf{p}_1 \int d\varphi_1 \; \hat{\mathbf{u}}_1 \; f^{(1)}(\mathbf{r}_1,\mathbf{p}_1,\varphi_1,t).\end{aligned} \tag{2.5}$$

The goal is now to reduce the equation for $f^{(1)}$ to equations for the mean fields and simplify the problem further from there. Eq. (2.4) may be integrated over $\mathbf{p}_1$ and φ_1 which yields the continuity equation for the number density

$$\frac{\partial \rho}{\partial t} + \nabla_{\mathbf{r}_1} \cdot \mathbf{j} = 0. \tag{2.6}$$

Similar, an equation for $\mathbf{j}$ can be found by multiplying Eq. (2.4) with $\mathbf{p}_1/m$ and then integrating over $\mathbf{p}_1$ and φ_1 to obtain

$$\begin{aligned}\frac{\partial \mathbf{j}}{\partial t} = &-\frac{1}{m^2}\int d\mathbf{p}_1 \int d\varphi_1 \; \mathbf{p}_1 \left(\mathbf{p}_1 \cdot \nabla_{\mathbf{r}_1}\right) f^{(1)} - \gamma\,\mathbf{j} + \frac{1}{m}\,\rho\,\mathbf{F}^{\text{ext}}\\ &+ \frac{1}{m}\int d\mathbf{r}_2 \; \mathbf{F}^{(2)}\,\rho^{(2)} + \frac{f_0}{m}\,\rho\,\mathbf{P}.\end{aligned} \tag{2.7}$$

Here the two body number density

$$\rho^{(2)}(\mathbf{r}_1,\mathbf{r}_2,t) = \int d\mathbf{p}_1 \int d\mathbf{p}_2 \int d\varphi_1 \int d\varphi_2 \; f^{(2)}(\mathbf{r}_1,\mathbf{r}_2,\mathbf{p}_1,\mathbf{p}_2,\varphi_1,\varphi_2,t) \tag{2.8}$$

is used in the interaction integral.
Now, effectively the same two approximations as in [43] are made to proceed further. The only difference is the dependence of $f^{(1)}$ on φ_1. First, the interaction integral containing the two body number density is approximated via

$$\int d\mathbf{r}_2 \; \mathbf{F}^{(2)}(\mathbf{r}_1,\mathbf{r}_2)\,\rho^{(2)}(\mathbf{r}_1,\mathbf{r}_2) = -\rho(\mathbf{r}_1)\,\nabla_{\mathbf{r}_1}\frac{\delta \mathcal{F}_{exc}[\rho]}{\delta \rho(\mathbf{r}_1)} \tag{2.9}$$

which is exact only in equilibrium. Therefore, the commonly used approximation is to use this expression also in the non-equilibrium case [44]. $\mathcal{F}_{exc}$ is the excess free energy which contains energy contributions due to particle interactions. The second approximation is

to assume that the $\mathbf{p}_1$ and φ_1 dependencies in $f^{(1)}$ decouple and that the momentum part takes the 'local-equilibrium' Maxwell-Boltzmann form [45]. The latter assumes that momentum is gaussian distributed around the local mean $\overline{\mathbf{p}_1} = m\,\mathbf{v}(\mathbf{r}_1, t)$ where $\mathbf{v}$ is the local average particle velocity, analogous to the local mean orientation $\mathbf{P}$. Therefore the one bode density can be written as

$$f^{(1)}(\mathbf{r}_1, \mathbf{p}_1, \varphi_1, t) = \frac{\Phi(\mathbf{r}_1, \varphi_1, t)}{2\pi m k T}\ \exp\left(-\frac{(\mathbf{p}_1 - m\,\mathbf{v})^2}{2mkT}\right) \tag{2.10}$$

where $\Phi(\mathbf{r}_1, \varphi_1, t)$ is the part containing the orientational dependence and kT is the thermal energy. With this form of the one body density it follows from the definition of the mean field densities that

$$\begin{aligned} \rho(\mathbf{r}_1, t) &= \int d\varphi_1\ \Phi(\mathbf{r}_1, \varphi_1, t) \\ \mathbf{j}(\mathbf{r}_1, t) &= \rho(\mathbf{r}_1, t)\,\mathbf{v}(\mathbf{r}_1, t). \end{aligned} \tag{2.11}$$

Applying now the approximations Eq. (2.9) and Eq. (2.10) to the current equation in Eq. (2.7) results in an dynamical equation for $\mathbf{v}$ which only depends on the other mean fields. This calculation is done and described in [43] and therefore not rewritten here. All terms originating from the additional particle orientation vanish up to a coupling term in the momentum equation, which does not change the principal calculation but is also found again in the resulting mean velocity equation

$$\frac{\partial \mathbf{v}}{\partial t} + (\mathbf{v}\cdot\nabla)\mathbf{v} = -\gamma\,\mathbf{v} - \frac{1}{m}\nabla\frac{\delta\mathcal{F}[\rho]}{\delta\rho} + \frac{f_0}{m}\,\mathbf{P}. \tag{2.12}$$

Diffusion, interactions with other particles and with external fields are summarized here under the Helmholtz free energy functional [45]

$$\mathcal{F}[\rho] = kT\int d\mathbf{r}\ \rho(\mathbf{r})\ [\ln(\Lambda\rho(\mathbf{r})) - 1] + \mathcal{F}_{exc}[\rho] + \int d\mathbf{r}\ \rho(\mathbf{r})\,V^{\text{ext}}(\mathbf{r}). \tag{2.13}$$

The first term is the ideal gas free energy with the thermal wave length Λ which is irrelevant in the current context, since it vanishes when the functional derivative is taken in the dynamical equation of $\mathbf{v}$.

Next, a dynamical equation for the mean orientation $\mathbf{P}$ can be found by first multiplying Eq. (2.4) for the one body density with $\hat{\mathbf{u}}_1$ and then integrating over $\mathbf{p}_1$ and φ_1. The resulting terms for the dynamical equation of $\mathbf{P}$ are calculated in the following separately. First, the left hand side of Eq. (2.4) is converted by using the continuity Eq. (2.6) and the expression for the current in Eq. (2.11). This yields

$$\frac{\partial(\rho\mathbf{P})}{\partial t} = \rho\,\frac{\partial\mathbf{P}}{\partial t} - \rho\,\mathbf{P}\,\nabla\cdot\mathbf{v} - \mathbf{P}\,(\mathbf{v}\cdot\nabla\rho). \tag{2.14}$$

Next, the first term on the right hand side is simplified with the approximation of the one body density Eq. (2.10) to

$$\frac{1}{m}\int d\mathbf{p}_1 \int d\varphi_1\ \hat{\mathbf{u}}_1\,(\mathbf{p}_1\cdot\nabla_{\mathbf{r}_1})\,f^{(1)} = \rho\,(\mathbf{v}\cdot\nabla)\mathbf{P} + \mathbf{P}(\mathbf{v}\cdot\nabla\rho) + \rho\,\mathbf{P}\,\nabla\cdot\mathbf{v}. \tag{2.15}$$

Like for the pair interaction in the current equation the interaction term for the orientation is now also approximated via an equilibrium excess functional

$$\begin{aligned} &\int d\mathbf{r}_2 \int d\mathbf{p}_2 \int d\varphi_2\ G^{(2)}(\mathbf{r}_1,\mathbf{r}_2,\varphi_1,\varphi_2)\ f^{(2)}(\mathbf{r}_1,\mathbf{r}_2,\mathbf{p}_1,\mathbf{p}_2,\varphi_1,\varphi_2) \\ =& -f^{(1)}(\mathbf{r}_1,\mathbf{p}_1,\varphi_1)\ \partial_{\varphi_1}\frac{\delta\mathcal{F}_{exc}[f^{(1)}]}{\delta f^{(1)}} \end{aligned} \tag{2.16}$$

leading to the expression for the orientational interaction

$$\begin{aligned} &-\int d\mathbf{r}_2 \int d\varphi_1 \int d\varphi_2\ \hat{\mathbf{u}}_1\,\partial_{\varphi_1}\Big(G_2(\mathbf{r}_1,\mathbf{r}_2,\varphi_1,\varphi_2)\,f^{(2)}(\mathbf{r}_1,\mathbf{r}_2,\varphi_1,\varphi_2,t)\Big) \\ =& -\int d\varphi_1\,(\partial_{\varphi_1}\hat{\mathbf{u}}_1)\ \ \Phi(\mathbf{r}_1,\varphi_1)\ \partial_{\varphi_1}\frac{\delta\mathcal{F}_{exc}[\Phi]}{\delta\Phi} \\ =& -\rho\frac{\delta\mathcal{F}_P[\mathbf{P}]}{\delta\mathbf{P}}. \end{aligned} \tag{2.17}$$

In the first line the momentum integrations are already carried out which is why the two body density no longer depends on them. To arrive at the second line partial integration on φ_1 is used and the approximation Eq. (2.16) is inserted. In the last step the excess functional $\mathcal{F}_{\text{exc}}[\Phi] = \mathcal{F}_P[\mathbf{P}[\Phi]]$ is expressed via the mean orientation $\mathbf{P}$ by applying the chain rule for functional differentiation

$$\frac{\delta \mathcal{F}_{\text{exc}}\left[\mathbf{P}[\Phi]\right]}{\delta \Phi(\mathbf{r},\varphi,t)} = \int d\mathbf{r}' \int dt' \, \frac{\delta \mathcal{F}_P[\mathbf{P}]}{\delta \mathbf{P}(\mathbf{r}',t')} \, \frac{\delta \mathbf{P}[\Phi](\mathbf{r}',t')}{\delta \Phi(\mathbf{r},\varphi,t)} = \frac{\delta \mathcal{F}_P[\mathbf{P}]}{\delta \mathbf{P}(\mathbf{r},t)} \hat{\mathbf{u}}(\varphi). \tag{2.18}$$

Here, $\mathbf{P}[\Phi]$ is given by inserting the approximation for $f^{(1)}$ Eq. (2.10) into the definition of $\mathbf{P}$ Eq. (2.5) which yields

$$\mathbf{P}[\Phi] = \int d\varphi \; \hat{\mathbf{u}} \, \Phi(\mathbf{r},\varphi,t). \tag{2.19}$$

All over terms in the resulting dynamical equation of $\mathbf{P}$ ever vanish or are dealt with via partial integration. Together with the continuity Eq. (2.6), the velocity Eq. (2.12) and the average one particle torque $\overline{\mathbf{G}^{(1)}} = \int d\varphi \, (\partial_\varphi \hat{\mathbf{u}}) \, G^{(1)} \, \Phi$, the final form of the model for underdamped active systems then reads

$$\begin{aligned} \frac{\partial \rho}{\partial t} &= -\nabla \cdot (\rho \mathbf{v}) \\ \frac{\partial \mathbf{v}}{\partial t} + (\mathbf{v} \cdot \nabla)\mathbf{v} &= -\gamma \, \mathbf{v} - \frac{1}{m} \nabla \frac{\delta \mathcal{F}}{\delta \rho} + \gamma v_0 \mathbf{P} \\ \frac{\partial \mathbf{P}}{\partial t} + (\mathbf{v} \cdot \nabla)\mathbf{P} &= -D_R \mathbf{P} - \frac{\delta \mathcal{F}_P}{\delta \mathbf{P}} + \overline{\mathbf{G}^{(1)}}. \end{aligned} \tag{2.20}$$

The mean $\overline{\mathbf{G}^{(1)}}$ describes a particle's behaviour of orienting independently of other particles' orientations. In principle, this term can also be written in functional form analogous to the one particle force $\mathbf{F}^{(1)}$. For the context of the next section it is however formulated separately in the mean torque form. Generally, the particle interactions do not need to be formulated in a functional form. However, in the context of active matter models this conceptual connection to equilibrium physics proofs to be a useful and instructive ansatz [4, 21]. But closure relations for the two body or higher order densities needed for particle interactions can also be found differently [30]. The model for underdamped active systems Eq. (2.20) now serves as the basis for the choice of concrete systems to be investigated.

2.2. Underdamped Active Crystals

The first system to be formulated is inspired by the work of Menzel *et al.* on active crystals in the overdamped regime [19, 20] which is described in Ch. 1.3. The unspecified terms in Eq. (2.20) are chosen such that in the limit $m \to 0$ the overdamped active crystal model Eq. (1.4) is recovered. Therefore it is expected that results of the latter are reproduced within this generalized underdamped model for small mass. Consequently the functionals and the mean one body torque are set to

$$\begin{aligned} \mathcal{F}[\rho] = \mathcal{F}_{\mathrm{PFC}} &= \int d\mathbf{r}\, \frac{\rho}{2}\left[\epsilon + \lambda\left(q_0^2 + \nabla^2\right)^2\right]\rho + \frac{u}{4}\,\rho^4 \\ \mathcal{F}_P[\mathbf{P}] &= \frac{C_1}{2}\int d\mathbf{r}\, \left(|\nabla P_x|^2 + |\nabla P_y|^2\right) \\ \overline{\mathbf{G}^{(1)}} &= -\frac{v_0}{|\overline{\rho}|}\,\nabla\rho. \end{aligned} \tag{2.21}$$

Translational interactions are given by the phase field crystal functional $\mathcal{F}_{\mathrm{PFC}}$, already visited in Ch. 1.2. Since it describes systems at high densities, the number density may be interpreted as variation around a high mean value which justifies a constant mobility approximation for the continuity equation in Eq. (2.20). The advective term $(\mathbf{v}\cdot\nabla)\,\mathbf{P}$ is dropped for now, since it changes the dynamics such that a simple particle interpretation of density peaks is not possible, as described later in Ch. 4.3. Next, it is observed that the orientational interaction functional $\mathcal{F}_P$ is conceptually equivalent to the Frank-Oseen free energy of liquid crystals with one bending constant C_1 [46]. For $C_1 > 0$, any kind of spatial inhomogeneities in the orientation field cost free energy. Therefore the system favours a uniform state in which all polar particles are aligned in the same direction. The one particle torque $\overline{\mathbf{G}^{(1)}}$ drives an instability from the isotropic state $\mathbf{P} = \mathbf{0}$ with the activity parameter v_0. The self-propulsion force is given by $f_0 = \alpha v_0$. With these ingredients the time evolution of the mean fields in the underdamped active crystal model reads

$$\begin{aligned} \frac{\partial\rho}{\partial t} &= -\,|\overline{\rho}|\,\nabla\cdot\mathbf{v} \\ \frac{\partial\mathbf{v}}{\partial t} + (\mathbf{v}\cdot\nabla)\,\mathbf{v} &= -\gamma\,\mathbf{v} - \frac{1}{m}\nabla\frac{\delta\mathcal{F}}{\delta\rho} + \gamma v_0\,\mathbf{P} \\ \frac{\partial\mathbf{P}}{\partial t} &= -D_R\,\mathbf{P} - \frac{\delta\mathcal{F}}{\delta\mathbf{P}} - \frac{v_0}{|\overline{\rho}|}\,\nabla\rho. \end{aligned} \tag{2.22}$$

By taking the overdamped limit $\gamma^{-1} \propto m \to 0$ the convective derivative on the left hand side of the velocity equation becomes negligible leading to the simplified form

$$\begin{aligned} \frac{\partial \rho}{\partial t} &= |\overline{\rho}| \left(\frac{1}{\alpha} \nabla^2 \frac{\delta \mathcal{F}}{\delta \rho} - v_0 \nabla \cdot \mathbf{P} \right) \\ \frac{\partial \mathbf{P}}{\partial t} &= -D_R \, \mathbf{P} - \frac{\delta \mathcal{F}}{\delta \mathbf{P}} - \frac{v_0}{|\overline{\rho}|} \nabla \rho \end{aligned} \tag{2.23}$$

which coincides with the overdamped model by Menzel *et al.* [19, 20] up to rescaling, as intended.
In order to extract the physically relevant parameters and to numerically implement the under- and overdamped model, Eqs. (2.22) and (2.23) are non-dimensionalized. A quantity x' is rescaled with a factor Y to its corresponding dimensionless form like $x = x'/Y$ which is depicted as $x' \to Y \cdot x$. For simplicity of notation, the same symbol is used for x' and x in the following. The used rescaling rules read

$$\begin{array}{llll} \mathbf{r} \to q_0 \, \mathbf{r} & t \to T \, t & \rho \to (\lambda q_0^4 u^{-1})^{1/2} \, \rho & \overline{\rho} \to (\lambda q_0^4 u^{-1})^{1/2} \, \overline{\rho} \\ \mathbf{v} \to \dfrac{1}{T q_0} \, \mathbf{v} & \epsilon \to \lambda q_0^4 \, \epsilon & m \to \xi^{-1} \alpha T \, m & v_0 \to \dfrac{1}{T q_0} \, v_0 \\ C_1 \to \dfrac{1}{T q_0^2} \, C_1 & D_R \to \dfrac{1}{T} \, D_R & T = \dfrac{\alpha u^{1/2}}{(\lambda q_0^4)^{3/2} q_0^2 \xi} & \end{array} \tag{2.24}$$

where the arbitrary dimensionless number ξ is solely introduced for convenience of the numerical implementation as explained in Ch. 3.2. From this the dimensionless form for the underdamped model equations follows as

$$\begin{aligned} \frac{\partial \rho}{\partial t} &= - |\overline{\rho}| \, \nabla \cdot \mathbf{v} \\ \frac{\partial \mathbf{v}}{\partial t} + (\mathbf{v} \cdot \nabla) \, \mathbf{v} &= \frac{1}{m} \left(-\xi \, \mathbf{v} - \nabla \left[\left(\epsilon + \left(1 + \nabla^2 \right)^2 \right) \rho + \rho^3 \right] + \xi v_0 \, \mathbf{P} \right) \\ \frac{\partial \mathbf{P}}{\partial t} &= \left(C_1 \nabla^2 - D_R \right) \mathbf{P} - \frac{v_0}{|\overline{\rho}|} \nabla \rho. \end{aligned} \tag{2.25}$$

Here it becomes clear that the mass m serves as a control parameter which determines the damping regime. For low m the forces on the right hand side of the velocity equation determine quasi instantaneously the direction of movement. Therefore the system is in

the overdamped regime. For larger m a change of the current velocity takes longer, which corresponds to the underdamped regime.
With the same rescaling rules the dimensionless form of the overdamped limit equations reads

$$\begin{aligned} \frac{\partial \rho}{\partial t} &= \frac{|\overline{\rho}|}{\xi} \nabla^2 \left[\left(\epsilon + \left(1 + \nabla^2 \right)^2 \right) \rho + \rho^3 \right] - v_0 \nabla \cdot \mathbf{P} \\ \frac{\partial \mathbf{P}}{\partial t} &= \left(C_1 \nabla^2 - D_R \right) \mathbf{P} - v_0 \nabla \rho \end{aligned} \tag{2.26}$$

where additionally the factor $|\overline{\rho}|$ got included in the orientation field $|\overline{\rho}|\,\mathbf{P} \rightarrow \mathbf{P}$. The Eqs. (2.25) and (2.26) are numerically implemented as described in Ch. 3.2 and the physical results observed in the model are discussed in Ch. 4.

2.3. PFC Alignment

Many microscopic active systems, like dense suspensions of bacteria or microswimmers, exhibit a large variety of collective effects like vorticity patterns or turbulent-like states [39, 40, 47]. The key ingredients to their phenomenological description within coarse grained continuum theories is the description of a preferred emergent length scale and the local alignment of self-propulsion directions. Typically this is formulated in terms of an incompressible velocity field $\mathbf{v}$ whose time evolution includes commonly used expressions like

$$\frac{\partial \mathbf{v}}{\partial t} = (\kappa - \beta\,|\mathbf{v}|^2)\,\mathbf{v} + \Gamma_0\,\nabla^2\mathbf{v} + \Gamma_2\left(\nabla^2\right)^2\mathbf{v} + ... \tag{2.27}$$

plus additional terms depending on the model. The κ and β terms were originally introduced by Toner and Tu [22] for the description of flocking in active systems. For $\kappa < 0$ the system is in an unordered isotropic state $\mathbf{v} = \mathbf{0}$, while for $\kappa > 0$ local alignment of orientations causes a net velocity amplitude $\sqrt{\kappa/\beta}$. The Swift-Hohenberg like Γ terms describe pattern formation in the velocity field with an characteristic length scale $l_0 = 2\pi\sqrt{2\Gamma_2/\Gamma_0}$ [17]. This minimal approach is extended in different variations in order to predict the collective behaviour of microscopic systems [29, 39, 40, 47–49].
Guided by the spirit of this work to investigate the role of inertia in active systems, the minimal approach Eq. (2.27) is used to specify a corresponding underdamped system. The focus then lies on the arising consequences of introducing inertia. Therefore the interaction functionals are chosen as

$$\begin{aligned}
\mathcal{F}[\rho] &= \int d\mathbf{r}\ \frac{c}{2}\,\rho^2 \\
\mathcal{F}_P[\mathbf{P}] &= \int d\mathbf{r}\ \frac{\mathbf{P}}{2}\left[-a + \lambda\left(q_0^2 + \nabla^2\right)^2\right]\mathbf{P} + \frac{\beta}{4}\,|\mathbf{P}|^4 \\
\overline{\mathbf{G}^{(1)}} &= 0.
\end{aligned} \tag{2.28}$$

Note that the orientation interaction takes the form of a (vectorial) PFC functional, like also used for the density field in the active crystal model. However, here its terms have a distinct physical interpretation. This becomes more apparent from inserting into Eq. (2.20) which yields the dynamical equations

$$\begin{aligned} \frac{\partial \rho}{\partial t} &= -\nabla \cdot (\rho\, \mathbf{v}) \\ \frac{\partial \mathbf{v}}{\partial t} + (\mathbf{v} \cdot \nabla)\, \mathbf{v} &= -\gamma\, \mathbf{v} - \frac{c}{m}\, \nabla \rho + \gamma v_0\, \mathbf{P} \\ \frac{\partial \mathbf{P}}{\partial t} + (\mathbf{v} \cdot \nabla)\, \mathbf{P} &= (\kappa - \beta\, |\mathbf{P}|^2)\, \mathbf{P} - \lambda \left(q_0^2 + \nabla^2\right)^2\, \mathbf{P} \end{aligned} \tag{2.29}$$

with $\kappa = a - D_R$. As intended, the time evolution of the orientation resembles Eq. (2.27). First, the Toner-Tu terms (κ, β) can be identified. In the locally aligned state $\kappa > 0$, the alignment strength a is higher than rotational diffusion. And correspondingly for high enough D_R, the system favours the isotropic state $\mathbf{P} = \mathbf{0}$. And second, the length scale term λ is a special case of the formulation in Eq. (2.27) for $\Gamma_0 = 2\lambda q_0$ and $\Gamma_2 = \lambda$. This form is chosen, since the strength of the interaction can easily be varied via λ while the preferred length scale $l_0 = 2\pi/q_0$ stays unaltered. Additional one body torques $G^{(1)}$ are neglected for simplicity. Further, the self-propulsion velocity $v_0 = f_0/\alpha$ corresponds to the steady state velocity of a particle in an environment with friction constant α and accelerated by the activity force f_0. In contrast to typical microscopic models which are incompressible, density variations are allowed here, reflected in the continuity equation. Therefore the specified model is appropriate to describe more dilute systems. High density regions normally tend to dissolve over time, which is expressed in the density gradient term in the velocity equation with compressibility parameter c.
As an important reference case, the overdamped limit of Eq. (2.29) is determined by taking $m \to 0$. Then the convective derivative on the left hand side of the velocity equation becomes irrelevant. Also the advection of $\mathbf{P}$ as a consequence of inertia is neglected. With this the dynamic in the overdamped limit simplifies to

$$\begin{aligned} \frac{\partial \rho}{\partial t} &= \frac{c}{2\alpha}\, \nabla^2 \rho^2 - v_0\, \nabla \cdot (\rho\, \mathbf{P}) \\ \frac{\partial \mathbf{P}}{\partial t} &= \left(\kappa - \beta\, |\mathbf{P}|^2\right)\, \mathbf{P} - \lambda \left(q_0^2 + \nabla^2\right)^2\, \mathbf{P}. \end{aligned} \tag{2.30}$$

As in the previous section, Eqs. (2.29) and (2.30) are non-dimensionalized in order to extract physically relevant parameters and for numerical implementation. The used rescaling rules read

$$\begin{array}{llll} \mathbf{r} \to q_0\ \mathbf{r} & t \to \kappa^{-1}\ t & \rho \to \dfrac{\alpha\kappa}{cq_0^2}\ \rho & \mathbf{v} \to \dfrac{\kappa}{q_0}\ \mathbf{v} \\ m \to \dfrac{\alpha}{\kappa}\ m & v_0 \to \dfrac{(\kappa\beta)^{1/2}}{q_0}\ v_0 & \mathbf{P} \to \left(\dfrac{\kappa}{\beta}\right)^{1/2}\ \mathbf{P} & \lambda \to \dfrac{\kappa}{q_0^4}\ \lambda. \end{array} \tag{2.31}$$

Applying those to the underdamped field equations yields their dimensionless form

$$\begin{aligned} \frac{\partial \rho}{\partial t} &= -\nabla \cdot (\rho\, \mathbf{v}) \\ \frac{\partial \mathbf{v}}{\partial t} + (\mathbf{v} \cdot \nabla)\, \mathbf{v} &= \frac{1}{m} \left(-\mathbf{v} - \nabla\rho + v_0\, \mathbf{P}\right) \\ \frac{\partial \mathbf{P}}{\partial t} + (\mathbf{v} \cdot \nabla)\, \mathbf{P} &= (1 - |\mathbf{P}|^2)\, \mathbf{P} - \lambda \left(1 + \nabla^2\right)^2\ \mathbf{P}. \end{aligned} \tag{2.32}$$

And the dimensionless overdamped limit equations follow as

$$\begin{aligned} \frac{\partial \rho}{\partial t} &= \frac{1}{2}\nabla^2\rho^2 - v_0\, \nabla \cdot (\rho\, \mathbf{P}) \\ \frac{\partial \mathbf{P}}{\partial t} &= \left(1 - |\mathbf{P}|^2\right)\ \mathbf{P} - \lambda \left(1 + \nabla^2\right)^2\ \mathbf{P}. \end{aligned} \tag{2.33}$$

The Eqs. (2.32) and (2.33) are numerically implemented as described in Ch. 3.3 and the physical results observed in the model are discussed in Ch. 5.

2.4. List of all Models

In order to serve the reader as an overview, all relevant models for the main chapters 4 and 5 are listed in the following table. Also, all model equations as they appear throughout this work are compactly summarized for comparison.

Table 2.1.: Overview of all discussed models with name and references to model equations and relevant chapter. Different non-equilibrium states, as they are denoted in the context of each model, are listed with their respective parameter regimes.

Model	v_0	m	State	Note
Overdamped Active Crystal Eq. (2.26), Ch. 4.1	< 0.3	-	resting crystal	Introduced by Menzel *et al.* [19, 20]. Mass parameter absent, since system completely overdamped.
	> 0.3	-	traveling crystal	
Underdamped Active Crystal Eq. (2.25), Ch. 4.2	< 0.3	0.1 - 2	resting crystal	Same steady states as Overdamped Active Crystal, but time scales of relaxation increase with m.
	> 0.3	0.1 - 2	traveling crystal	
Extendend Underdamped Active Crystal Eq. (4.11), Ch. 4.3	0.4	0.1, 2	decomposition	Underdamped Active Crystal with **P** advection. Constant and density dependent v_0 result in same states.
	$v_0(\rho)$	0.1, 2	decomposition	

Model	λ	v_0	m	State	Note
Overdamped PFC Alignment Eq. (2.33), Ch. 5.1	> 0.5	0.2	-	laning	Mass parameter absent, since system completely overdamped.
	< 0.5	0.2	-	vortex lattices	
Underdamped PFC Alignment Eq. (2.32), Ch. 5.2	> 0.2	0.2	0.1	laning	
	< 0.05	0.2	0.1	collective motion	
	0.1	0.1 - 0.2	0.1, 10	turbulence	

Overdamped Active Crystal model:

$$\begin{aligned} \frac{\partial \rho}{\partial t} &= |\overline{\rho}|\ \nabla^2 \left[\left(\epsilon + \left(1 + \nabla^2 \right)^2 \right) \rho + \rho^3 \right] - v_0 \nabla \cdot \mathbf{P} \\ \frac{\partial \mathbf{P}}{\partial t} &= \left(C_1 \nabla^2 - D_R \right) \mathbf{P} - v_0 \nabla \rho \end{aligned} \tag{2.34}$$

Underdamped Active Crystal model:

$$\begin{aligned} \frac{\partial \rho}{\partial t} &= -|\overline{\rho}|\ \nabla \cdot \mathbf{v} \\ \frac{\partial \mathbf{v}}{\partial t} + (\mathbf{v} \cdot \nabla)\, \mathbf{v} &= \frac{1}{m} \left(-\mathbf{v} - \nabla \left[\left(\epsilon + \left(1 + \nabla^2 \right)^2 \right) \rho + \rho^3 \right] + v_0 \, \mathbf{P} \right) \\ \frac{\partial \mathbf{P}}{\partial t} &= \left(C_1 \nabla^2 - D_R \right) \mathbf{P} - \frac{v_0}{|\overline{\rho}|} \nabla \rho. \end{aligned} \tag{2.35}$$

Extendend Underdamped Active Crystal model:

$$\begin{aligned} \frac{\partial \rho}{\partial t} &= -|\overline{\rho}|\ \nabla \cdot \mathbf{v} \\ \frac{\partial \mathbf{v}}{\partial t} + (\mathbf{v} \cdot \nabla)\, \mathbf{v} &= \frac{1}{m} \left(-\mathbf{v} - \nabla \left[\left(\epsilon + \left(1 + \nabla^2 \right)^2 \right) \rho + \rho^3 \right] + v_0 \, \mathbf{P} \right) \\ \frac{\partial \mathbf{P}}{\partial t} + (\mathbf{v} \cdot \nabla)\, \mathbf{P} &= \left(C_1 \nabla^2 - D_R \right) \mathbf{P} - \frac{v_0}{|\overline{\rho}|} \nabla \rho. \end{aligned} \tag{2.36}$$

Overdamped PFC Alignment model:

$$\begin{aligned} \frac{\partial \rho}{\partial t} &= \frac{1}{2} \nabla^2 \rho^2 - v_0 \nabla \cdot (\rho \, \mathbf{P}) \\ \frac{\partial \mathbf{P}}{\partial t} &= \left(1 - |\mathbf{P}|^2 \right) \mathbf{P} - \lambda \left(1 + \nabla^2 \right)^2 \ \mathbf{P}. \end{aligned} \tag{2.37}$$

Underdamped PFC Alignment model:

$$\begin{aligned} \frac{\partial \rho}{\partial t} &= -\nabla \cdot (\rho \, \mathbf{v}) \\ \frac{\partial \mathbf{v}}{\partial t} + (\mathbf{v} \cdot \nabla)\, \mathbf{v} &= \frac{1}{m} \left(-\mathbf{v} - \nabla \rho + v_0 \, \mathbf{P} \right) \\ \frac{\partial \mathbf{P}}{\partial t} + (\mathbf{v} \cdot \nabla)\, \mathbf{P} &= \left(1 - |\mathbf{P}|^2 \right) \mathbf{P} - \lambda \left(1 + \nabla^2 \right)^2 \ \mathbf{P}. \end{aligned} \tag{2.38}$$

3. Numerical Methods

3.1. General Setup

All simulations are performed within *C++* using the *fftw* library [50] via the *fftw++* wrapper and the *omp* library for parallelization of array operations. Data analysis and visualization are done in *python*.
A pseudo-spectral algorithm is used for numerical time iteration [51]. This means that linear terms in the dynamical equations are evaluated in Fourier space and all non-linear ones in real space, which are then also transformed into Fourier space for time stepping. The Fourier transformation of a function f is denoted as $\mathfrak{F}[f] = \widetilde{f}(\mathbf{k})$. The implementation of a pseudo-spectral algorithm is demonstrated with the PFC model Eq. (1.3). First, a Fourier transformation is applied to the rescaled dynamical equations, yielding

$$\begin{aligned} & \frac{\partial \psi}{\partial t} = \nabla^2 \left[-\epsilon + \left(1 + \nabla^2\right)^2 \psi + \psi^3 \right] \quad \Big| \, \mathfrak{F}[\,\cdot\,] \\ \Leftrightarrow \quad & \frac{\partial \widetilde{\psi}}{\partial t} = L \, \widetilde{\psi} + N(\widetilde{\psi}) \end{aligned} \tag{3.1}$$

where linear terms are summarized within the factor $L = -k^2 \left[\epsilon + (1 - k^2)^2 \right]$ and non-linear ones within $N(\psi) = -k^2 \, \mathfrak{F}\left[\psi^3\right]$. The identity $\mathfrak{F}\left[\nabla^n f\right] = (i\mathbf{k})^n \, \widetilde{f}$ for any natural number n is used here. The dynamical equation is now numerically implemented by discretizing the fields ψ and $\widetilde{\psi}$ on two dimensional regular grids with lateral number of grid points n_x, n_y and spacing dx, dy and $dk_x = \frac{2\pi}{n_x dx}, dk_y = \frac{2\pi}{n_y dy}$, respectively. The lateral box lengths $l_x = n_x \cdot dx$ and $l_y = n_y \cdot dy$ are chosen to match the hexagonal symmetry preferred by the PFC functional in the crystalline phase, since periodic boundary conditions are used. This means, that one lateral length is chosen as a multiple of $l_0 = \frac{2\pi}{q_0}$ and the second then needs to match a multiple of $l_0\sqrt{3}$. It is noted that the real space field ψ is purely real valued, so only one half of the complex $\widetilde{\psi}$ field needs to be explicitly known, due to the applicable symmetry relation $\widetilde{\psi}(-\mathbf{k}) = \widetilde{\psi}^*(\mathbf{k})$. Therefore, in practice

a $n_y \times \lfloor \frac{n_x}{2} \rfloor + 1$ array of values for $\widetilde{\psi}$ is used in computations and for the *fftw* Fourier transformations.
Time stepping is now implemented via a semi-implicit Euler discretization with a fixed step size Δt. Semi-implicit means that all non-linear terms are evaluated at the current discrete time step t (explicit) and the linear terms are evaluated at the next time step $t+1$ (implicit). With a simple first order approximation for the time derivative the iteration scheme for Eq. (3.1) then reads

$$\begin{aligned} \frac{\widetilde{\psi}_{t+1} - \widetilde{\psi}_t}{\Delta t} &= L\ \widetilde{\psi}_{t+1} + N(\psi_t) \\ \Leftrightarrow \widetilde{\psi}_{t+1} &= \frac{\widetilde{\psi}_t + \Delta t\ N\left(\mathfrak{F}^{-1}\left[\widetilde{\psi}_t\right]^3\right)}{1 - \Delta t\ L} \end{aligned} \tag{3.2}$$

where the operations $\mathfrak{F}^{-1}[\,\cdot\,]$ and $\mathfrak{F}[\,\cdot\,]$ now stand for the computation of the (inverse) discrete *fftw* Fourier transformation. The clear advantage of iterating the dynamical equation in Fourier space is that the high derivatives which occur in the PFC functional can be implemented as a simple multiplication with multiples of $\mathbf{k}$. Also periodic boundary conditions are naturally included since the Fourier transformation treats the discrete and finite fields as periodically continued in each direction.
All simulations are started from homogeneous initial conditions with added noise, which is homogeneously distributed in the range 10^{-4}. In the next parts, the iteration rules for the dynamical equations of the active crystal and PFC alignment model are given. In both cases convective non-linearities $(\mathbf{v}\cdot\nabla)\,\mathbf{P}$ and/or $(\mathbf{v}\cdot\nabla)\,\mathbf{v}$ are present. Different approaches for their computation are tested for numerical stability:

- Computing the derivatives in real space with a up to fourth order central difference scheme and evaluating the second factor as weighted average from the respective position and the (next) nearest neighbour grid points.
- Computing the derivatives in Fourier space and then transform backwards.
- A 2/3−rule for anti-aliasing, by setting the upper third of the Fourier spectrum in each term to zero before multiplying in real space.
- Third order upwind scheme for the computation of derivatives in real space [52].

The latter alternative proved to be most stable in convection dominated parameter

regimes and is therefore implemented in all simulations. The symbol ∇ is used in the next two sections to denote the computation of a discrete derivative via the third order upwind scheme.

3.2. Active Crystals

The under- and overdamped model equations (2.25) and (2.26) are numerically implemented as demonstrated in the last section. The iteration scheme of the discretized fields in Fourier space $\rho, \mathbf{v}, \mathbf{P} \xrightarrow{\mathfrak{F}[\cdot]} \widetilde{\rho}, \widetilde{\mathbf{v}}, \widetilde{\mathbf{P}}$ for the underdamped equations is then given by

$$\begin{aligned}
\widetilde{\rho}_{t+1} &= \widetilde{\rho}_t - |\overline{\rho}|\ \Delta t\ i\mathbf{k} \cdot \widetilde{\mathbf{v}}_{t+1} \\
\widetilde{\mathbf{v}}_{t+1} &= \left(1 + \frac{\Delta t}{m}\xi\right)^{-1} \left[\widetilde{\mathbf{v}}_t - \Delta t \left(\mathfrak{F}[(\mathbf{v}_t \cdot \nabla)\, \mathbf{v}_t] + \frac{i\mathbf{k}}{m} \left(L\ \widetilde{\rho}_t + \mathfrak{F}[\rho_t^3]\right) - \frac{v_0}{m}\, \xi\ \widetilde{\mathbf{P}}_{t+1}\right)\right] \\
\widetilde{\mathbf{P}}_{t+1} &= \frac{\widetilde{\mathbf{P}}_t - \Delta t\, v_0\, |\overline{\rho}|^{-1}\ i\mathbf{k}\ \widetilde{\rho}_t}{1 + \Delta t\, (C_1\, k^2 + D_r)}
\end{aligned} \tag{3.3}$$

where the linear PFC terms are summarized in $L = \left[\epsilon + (1 - k^2)^2\right]$. The higher order k terms in L are expected to damp high wave numbers in the velocity field. In the used explicit form this term however can overestimate this damping which leads to numerical artefacts. Lowering the time step to 10^{-4} does not resolve this issue. Instead, a threshold for the k values in the second term of L is introduced via the condition $\frac{\Delta t}{m}\left(1 - k^2\right)^2 < 1$, comparable to ref. [14]. Further, the factor ξ is introduced in the rescaling and set to $\xi = 0.2 < 1$ in order to reduce the numerical friction factor. This is done for convenience, as the relaxation from the homogeneous initial conditions sets in quicker then. And lastly, for high values of m, numerical errors arising from the convective term are less damped, leading to numerical instability. This is found for all tested implementations of convection listed in the last part. The issue is resolved by applying in each iteration step a low pass filter on $\widetilde{\mathbf{v}}$, which sets the highest ten percent of modes to zero along both directions in Fourier space, in order to avoid accumulation of errors there.
The overdamped model equations are implemented without low pass filter or threshold for k values in the PFC term L. Their iteration scheme for the discretized fields reads

$$\begin{aligned}\widetilde{\rho}_{t+1} &= \left(1+\frac{|\overline{\rho}|}{\xi}\,k^2\,L\right)^{-1}\left[\widetilde{\rho}_t-\Delta t\left(\frac{|\overline{\rho}|}{\xi}\,k^2\,\mathfrak{F}[\rho_t^3]+iv_0\;\mathbf{k}\cdot\widetilde{\mathbf{P}}_{t+1}\right)\right]\\ \widetilde{\mathbf{P}}_{t+1} &= \frac{\widetilde{\mathbf{P}}_t-\Delta t\,v_0\;i\mathbf{k}\;\widetilde{\rho}_t}{1+\Delta t\,(C_1\,k^2+D_r)}.\end{aligned} \tag{3.4}$$

$\xi = 0.2$ is used in all cases where under- and overdamped model are compared.

3.3. PFC Alignment

The under- and overdamped model equations (2.32) and (2.30) are numerically implemented as demonstrated in Ch. 3.1. The iteration scheme of the discretized fields in Fourier space $\rho, \mathbf{v}, \mathbf{P} \xrightarrow{\mathfrak{F}[\cdot]} \widetilde{\rho}, \widetilde{\mathbf{v}}, \widetilde{\mathbf{P}}$ for the underdamped equations is then given by

$$\begin{aligned}\widetilde{\rho}_{t+1} &= \widetilde{\rho}_t-\Delta t\;i\mathbf{k}\cdot\mathfrak{F}\left[\widetilde{\rho}_t\,\widetilde{\mathbf{v}}_{t+1}\right]\\ \widetilde{\mathbf{v}}_{t+1} &= \left(1+\frac{\Delta t}{m}\right)^{-1}\left[\widetilde{\mathbf{v}}_t-\Delta t\left(\mathfrak{F}[(\mathbf{v}_t\cdot\nabla)\,\mathbf{v}_t]+\frac{i\mathbf{k}}{m}\,\widetilde{\rho}_t-\frac{v_0}{m}\;\widetilde{\mathbf{P}}_{t+1}\right)\right]\\ \widetilde{\mathbf{P}}_{t+1} &= (1+\Delta t\,L)^{-1}\left[\widetilde{\mathbf{P}}_t-\Delta t\left(\mathfrak{F}\left[(\mathbf{v}_t\cdot\nabla)\,\mathbf{P}_t+P_t^2\;\mathbf{P}_t\right]\right)\right]\end{aligned} \tag{3.5}$$

where the linear PFC terms are summarized in $L = \left[\lambda\left(1-k^2\right)^2-1\right]$. For numerical stability of the non-linear continuity equation in the underdamped case, a low pass filter for $\widetilde{\rho}_t$ applied after each iteration step, in order to avoid the accumulation of numerical errors in the field. Like for the underdamped active crystal scheme, the low pass filter sets the highest ten percent of modes to zero for both directions in Fourier space. Lastly, the iteration scheme for the overdamped model equations reads

$$\begin{aligned}\widetilde{\rho}_{t+1} &= \widetilde{\rho}_t-\Delta t\left(\frac{1}{2}k^2\;\mathfrak{F}\left[\rho_t^2\right]+v_0\,i\mathbf{k}\cdot\mathfrak{F}\left[\widetilde{\rho}_t\,\widetilde{\mathbf{P}}_{t+1}\right]\right)\\ \widetilde{\mathbf{P}}_{t+1} &= (1+\Delta t\,L)^{-1}\left(\widetilde{\mathbf{P}}_t-\Delta t\;\mathfrak{F}\left[P_t^2\;\mathbf{P}_t\right]\right).\end{aligned} \tag{3.6}$$

4. Active Crystal Model

In the following results for the underdamped active crystal model introduced in Ch. 2.2 are presented and discussed. In the low mass regime, the overdamped active crystal model, described in Ch. 1.3 is recovered and on the other hand a different dynamical behaviour is found in the high mass regime. For clarity the dynamical equations for the underdamped active crystal model are stated here again:

$$\begin{aligned} \frac{\partial \rho}{\partial t} &= -\left|\overline{\rho}\right| \nabla \cdot \mathbf{v} \\ \frac{\partial \mathbf{v}}{\partial t} + \left(\mathbf{v} \cdot \nabla\right) \mathbf{v} &= \frac{1}{m} \left(-\mathbf{v} - \nabla \left[\left(\epsilon + \left(1 + \nabla^2\right)^2 \right) \rho + \rho^3 \right] + v_0 \, \mathbf{P} \right) \\ \frac{\partial \mathbf{P}}{\partial t} &= \left(C_1 \, \nabla^2 - D_R \right) \mathbf{P} - \frac{v_0}{\left|\overline{\rho}\right|} \nabla \rho. \end{aligned} \tag{4.1}$$

All shown simulations are performed in the resting/traveling hexagonal state with fixed parameters $(\overline{\rho}, \epsilon, C_1, D_R) = (-0.4, -0.98, 0.2, 0.1)$. The density peaks in ρ may be identified as particles and thus are named as such in physical contexts. However, this is only for convenience since also other interpretations are possible, like e.g. identifying a density peak with an accumulation of several particles. Periodic patterns of accumulated active particles are known to from [35]. Since the onset of crystallization in the density field from the initial supercooled liquid takes some time, all time resolved data which is shown starts at $t = 100$.

4.1. Retaining the Overdamped Limit

The underdamped active crystal model is formulated such, that it coincides with the overdamped one, introduced by Menzel *et al.* [19, 20], for vanishing particle mass. In the following the physical behaviour of the underdamped model in the low mass regime is summarized. It is found that the results of the overdemped model presented in Ch. 1.3 are retained.

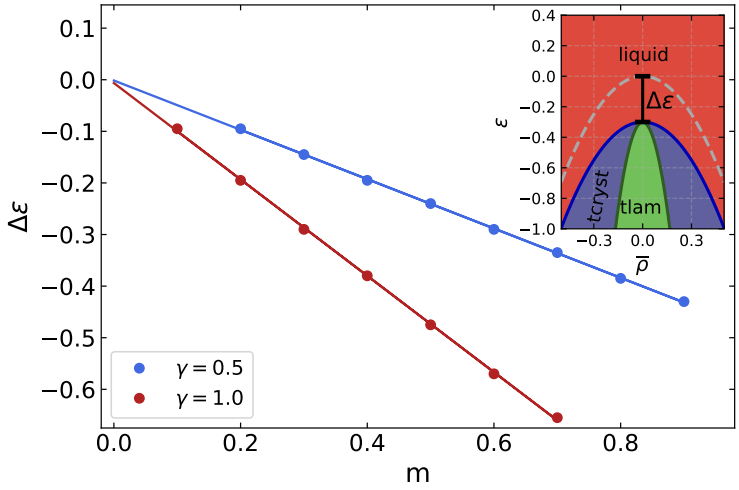

Fig. 4.1.: Parameter dependence of the state diagram temperature shift $\Delta\epsilon$ on m for two different γ values. The system is in the resting crystal state with $v_0 = 0.3$. For $m = 0$ the PFC force $\propto m^{-1}$ outweighs the active drive resulting in the unshifted state diagram $\Delta\epsilon = 0$ which is confirmed by the shown linear fits. Inset: Schematic drawing of a shifted state diagram with indicated temperature shift $\Delta\epsilon$ (after [19]). The dashed line corresponds to the unshifted liquid-solid phase boundary for passive particles.

Below the critical activity $v_{0,c}$, the system is in the resting crystal state. The kinetic energy input, due to activity of the particles, melts crystals close the the liquid-solid state boundary and therefore shifts the latter to lower temperatures. For this effective temperature shift the overdamped model predicts $\Delta\epsilon \propto v_0^2/C_1$, where $\Delta\epsilon$ is the temperature shift of the liquid-solid state boundary realative to the unshifted case of passive particles, as depicted in the inset of Fig. 4.1. Analogous to ref. [19], a linear stability analysis of the overdamped limit Eqs. (2.26) is performed (see App. A for details) resulting in

$$\Delta\epsilon \propto \frac{v_0^2}{C_1}\gamma m \tag{4.2}$$

where an additional dependence on the friction constant $\alpha = \gamma m$, not present in the overdamped model is predicted. To verify this also within the underdamped model the state boundary is located numerically. To this end, the underdamped model is rescaled differently as described in Eq. (2.24), to include the parameter dependence on γ and m

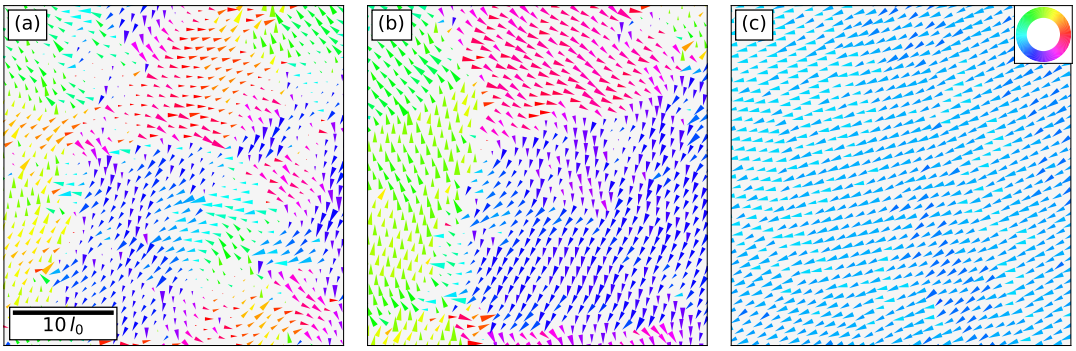

Fig. 4.2.: Coarse-graining of collectively moving clusters over time. The system is in the traveling hexagonal state $(m, v_0) = (0.1, 0.35)$. Density peaks are shown as arrows indicating peak velocity amplitude and color coded orientation. Clusters grow on the cost of others until in the long time limit one global propagation direction emerges. Simulation times are (a) 100, (b) 300 and (c) 1000. Only a part of the simulation box is shown.

explicitly. The changed rescaling rules are $t \to Tt$, $m \to T^2\lambda^{3/2}q_0^8u^{-1/2}m$ and $\gamma = T^{-1}\gamma$. With these, the rescaled velocity equation now reads

$$\frac{\partial \mathbf{v}}{\partial t} + (\mathbf{v}\cdot\nabla)\,\mathbf{v} = -\gamma\,\mathbf{v} - \frac{1}{m}\,\nabla\frac{\delta\mathcal{F}}{\delta\rho} + \gamma v_0\,\mathbf{P}. \tag{4.3}$$

The other rescaling rules and resulting dynamical equations do not change in this context and the time rescaling T is arbitrary. Note that this rescaling is only used to verify the technical parameter dependence of $\Delta\epsilon$ in Eq. (4.2). In the original rescaling the damping parameter γ is eliminated by choosing a time scale T. For fixed $\overline{\rho} = -0.4$, the liquid-solid state boundary is then located at the highest ϵ value for which crystalline structures are still observed. It can be seen in Fig. 4.1 that the linear dependence $\Delta\epsilon \propto \gamma m$, predicted from the overdamped limit equations is also observed in the underdamped model. For $m = 0$, the two shown linear fits cross at $\Delta\epsilon = 0$, meaning that the unshifted phase diagram of passive particles is predicted here. That is because the active force $\gamma v_0\,\mathbf{P}$ is outweighed by the PFC force $\propto m^{-1}$ for $m \to 0$ in this parametrisation.
Above the critical value $v_{0,c}$, the state diagram is not shifted further to lower temperatures. Instead, the additional kinetic energy input from the activity is used for translational self-propulsion. In this regime the instantaneous particle velocities, measured from peak displacements, give insight into the dynamical behaviour of the system.

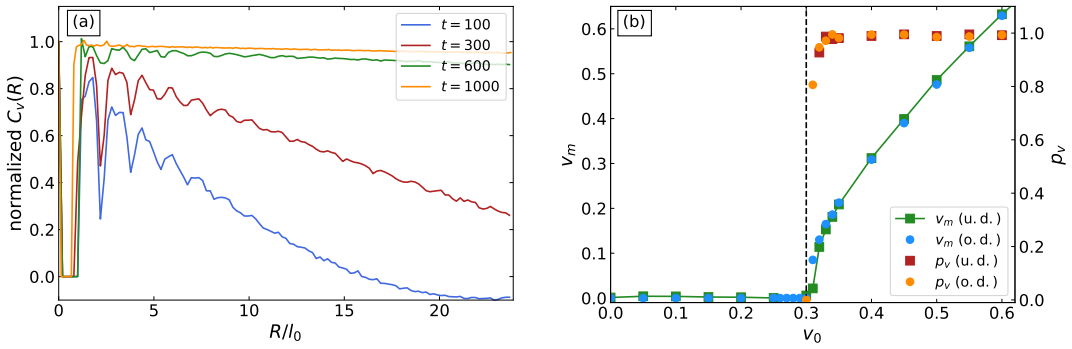

Fig. 4.3.: (a): The sample-averaged particle velocity correlation increases over time. In the long time limit the correlation length diverges, indicating global orientational order. The negative correlation at short times is due to many smaller antialigned and translationally moving clusters. Parameters read $(m, v_0) = (0.1,\ 0.35)$. (b): Sample-averaged velocity amplitude v_m and orientational order p_v in the long time limit for underdamped (u.d.) and overdamped (o.d.) model, respectively. In both cases the system spontaneously undergoes a transition from the resting into the traveling state at the critical activity $v_{0,c} \approx 0.3$ (dashed line). The mass in the underdamped model is $m = 0.1$.

When started from homogeneous initial conditions, there is no preferred direction of movement. But over time, smaller translationally moving clusters form due to local alignment of orientations. As can be seen in Fig. 4.2, these clusters continue to grow on the cost of others. In the long time limit, the system is in a steady state in which a swarm with one global migration direction has formed. The coarse graining process is also reflected in an increasing and finally diverging correlation length of the sample-averaged velocity correlation

$$C_v(R) = \overline{\mathbf{v}(\mathbf{r}) \cdot \mathbf{v}(\mathbf{r} + \mathbf{R})} \tag{4.4}$$

which is shown in Fig. 4.3 (a) for the particle velocities from Fig. 4.2.
The final steady state is characterized by the sample-averaged peak velocity amplitude v_m and orientational order p_v, defined in Ch. 1.3. It can be seen in Fig. 4.3 (b), that the underdamped model satisfactorily reproduces the final states of the overdamped one. Below the critical activity $v_{0,c} \approx 0.3$ the crystalline structures are at rest. For higher activities traveling crystals form, whose velocity increases with v_0 while the orientational

order has its maximum value $p_v = 1.0$, indicating global orientational order.

4.2. Underdamped Collective Dynamics

Methods

Measuring particle velocities via displacements of peak positions is a useful way to characterize the dynamics and final steady state in the overdamped crystal model. By adjusting the time difference between two used density field snapshots the displacements of particles are always large enough compared to the resolution of the simulation grid, but also small enough so that the right density peaks can be associated with one particle. Therefore, this migration method relies on a sufficiently sharp distribution of velocity amplitudes. While unproblematic in the overdamped model and in the overdamped regime of the underdamped model, the velocities show in general a larger variance in the underdamped regime of the underdamped model, where inertia becomes increasingly relevant. Another problem in this regime is the less stable hexagonal structure of the density field, as can be seen in Fig. 4.4 (a). Neighboring peaks can be less distinguishable lateral to their propagation direction and almost form density bands in which particles are delocalized. On the timescale between two simulation snapshots needed for the migration method, the peak positions on such a band can fluctuate substantially in lateral direction, leading to unrealistic particle velocity amplitudes and directions. More specifically, it is expected that at least locally particles align due to the free energy cost of spatial inhomogenities in the orientation field. This can for example be seen in the movie *ActiveCrystal.mp4*, which is attached to this thesis and described in App. B. The 'noisy' particle velocities in Fig. 4.4 (b) illustrate the described shortcomings of the migration method.

For the analysis of the underdamped model, another possibility to compute the particle velocities is chosen. In this 'net method' the particle positions are determined like in the previous method as density maxima, but with an additional threshold of $\rho_1 = 0.6$ to filter out local maxima at low densities in fluctuating regions. Then, the volume V of a particle is defined as the set of all grid points close to this position with a ρ value above a fixed threshold $\rho_0 = 0.1$. Here, close to means a maximum distance of $r_0 = 0.7\, l_0$ to avoid unrealistically high volumes. Also r_0 is the minimal distance allowed between two density peaks. Peaks closer than this value are associated with only one particle. Instead of measuring the displacements of density peaks between two snapshots, the flow field $\mathbf{v}$ in one snapshot is averaged over the volume V_i of the i-th particle leading to its respective momentary velocity

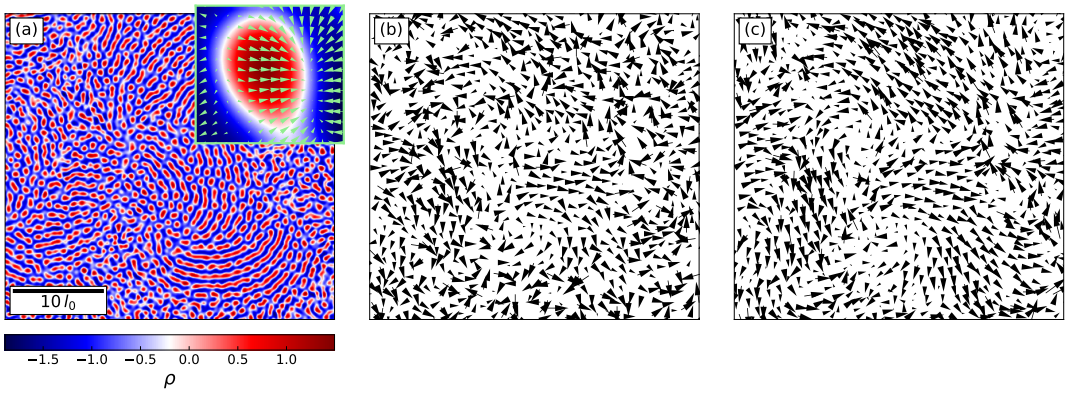

Fig. 4.4.: (a): Density field of a system in the underdamped regime $(m, v_0) = (2.0, 0.4)$. During this intermediate simulation time $t = 500$ particles are locally aligned, but high inertia destabilizes the translationally moving clusters observed in the overdamped regime. Only a part of the simulation box is shown. The inset illustrates the typical velocity field around a traveling density peak. (b): Particle velocities determined with the migration method. The expected local alignment of particle velocities is overlaid with orientational noise. (c): The same region analyzed with the net method demonstrates the improved detection of locally aligned velocities. All shown velocity fields are rescaled for better visibility.

$$\mathbf{v}_{net,i} = \frac{1}{|V_i|} \sum_{\mathbf{r} \in V_i} \mathbf{v}(\mathbf{r}). \tag{4.5}$$

In principle the number of particles and their velocity field $\mathbf{v}_{net}$ depends on the technical threshold values ρ_0, ρ_1. But the PFC functional with fixed ϵ parameter for all simulations produces the same peak-to-peak amplitude in the density field, which is large compared to the threshold values. Therefore the exact value of the latter is not very influential on the computed particle velocities.

With this net method approach the above described shortcomings of the migration method can be circumvent. Especially the local alignment of particles is captured, as illustrated in Fig. 4.4 (c). Also the detection efficiency of particles is higher. The migration method detects approximately 10% less particles in the underdamped regime, due to the described fluctuations along aligned particles which resemble density bands. Another advantage of the net method is the possibility to compute a net orientation for each particle by averaging $\mathbf{P}$ instead of $\mathbf{v}$ over particle areas. It is further noted that the absolute values of particle velocities computed with the net method, coincide with

the real velocities only up to a factor which depends on the model parameters like v_0 and m. Since the velocity field $\mathbf{v}$ around a density peak is maximal exactly at the peak area where $\mathbf{v}$ is averaged, v_{net} overestimates the actual particle velocity in the sense of peak displacement. In Fig. 4.5 this is shown be means of the sample-averaged particle velocity amplitude. But for the following discussion of the results the absolute values of velocities are irrelevant, since only relative values are used.

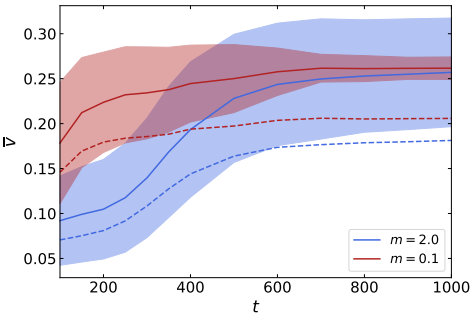

Fig. 4.5.: Sample-averaged velocity amplitude computed with net and migration method, solid and dashed lines respectively. The values differ by approximately the same factor for fixed parameters. Also shown is the standard deviation for the net method which decreases quickly in the overdamped regime compared to the opposite underdamped regime. The activity is $v_0 = 0.35$.

Which method is used to determine particle velocities also influences global system quantities like the equal-time velocity correlation $C_v(R)$ which is shown in Fig. 4.6 for the underdamped regime. In the case of lower activities the above described shortcomings of the migration method are negligible and both methods lead to similar results. On the other hand, for higher activities the typical hexagonal structure in ρ is less stable. The hereby introduced orientational noise in the migration method lowers its velocity correlation amplitude relative to the net method results. The insets in Fig. 4.6 quantify this noise in terms of the probability density of the angle φ between the velocity vectors of a particle, computed with both methods respectively. At lower activity φ quickly decreases while for higher activity values of up to 90° are typically be observed for all times.

Results

Independent of the mass parameter the system ends up in the traveling crystal state in the long time limit. Therefore, introducing inertia into the system does not qualitatively change the non-equilibrium state. What indeed changes is the time scale of the relaxation process to the steady state, which considerably increases with the mass parameter. This is reflected in the relaxation of the average particle velocity to its maximum in Fig. 4.5. The increase of the relaxation time with m is expected since frictional and active forces

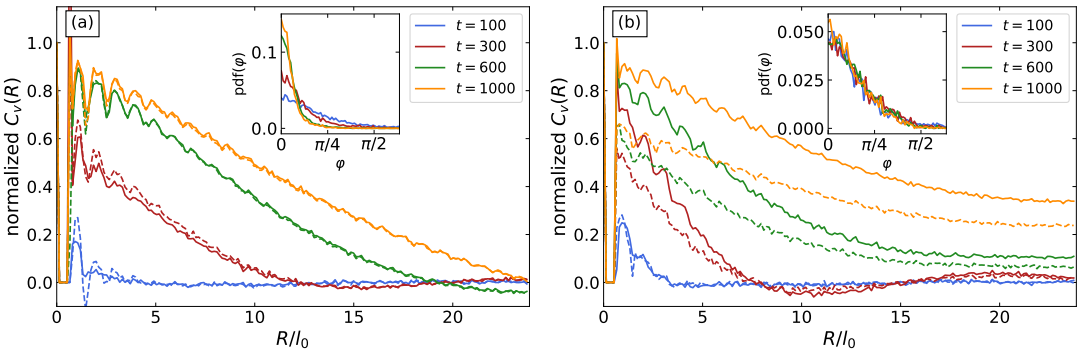

Fig. 4.6.: (a): Sample-averaged spatial velocity correlation function for particle velocities computed with the net and migration method, solid and dashed lines respectively. Shown are results in the underdamped regime $m = 2$ with (a) $v_0 = 0.35$ and (b) $v_0 = 0.4$. The correlation can get negative, indicating anti-alignment. The lowered correlation for the migration method in (b) originates from orientational noise which is quantified in the insets in terms of the probability density of the angle φ between the velocity vectors of a particle computed with both methods.

driving the velocity amplitude $\dot{\mathbf{v}} \propto \gamma(v_0 \mathbf{P} - \mathbf{v})$ include the time scale $\gamma^{-1} = m/\alpha$. However, additional collective effects arising from particle interactions further influence the relaxation behaviour of the system in dependence of the inertial regime. In the following it is focused on the underlying collective effects contributing to the dynamics of the system.

Typical particle velocity patterns, like the ones shown in Fig. 4.4, suggest that the underdamped regime is not only characterized by translationally moving clusters of particles but also by rotational ones. Differentiating these two states of collective motion helps to explain the velocity correlations in Fig. 4.6. For a better understanding the latter may be explained from two contributions. First, an exponentially decreasing part with a length scale corresponding to the translational cluster size. And second, an oscillating contribution with a period resulting from the rotating cluster radius. Depending on time, one contribution is more relevant than the other. E.g. for $v_0 = 0.4$ at $t = 300$ the correlation length of translational clusters is low, so the oscillating part at higher length scales becomes visible.

Circulation. The role of the rotating clusters for the collective dynamics is characterized in more detail in the following. A quantity which will prove to be useful for this is the

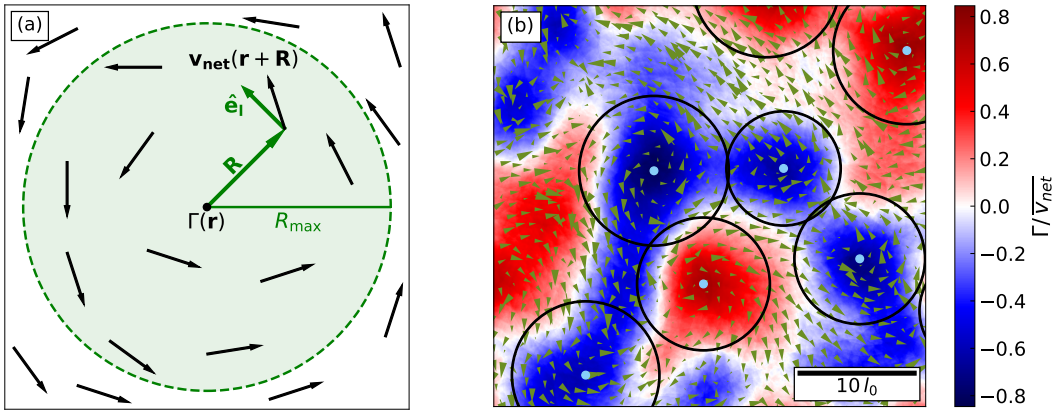

Fig. 4.7.: (a): Sketch for the definition of the circulation $\Gamma(\mathbf{r})$. All particle velocities $\mathbf{v}_{net}$ within the distance $R_{\max}$ are projected into the angular direction $\hat{\mathbf{e}}_l \perp \mathbf{R}$ and then averaged. (b): Circulation of particle velocities which are also shown in Fig. 4.4. Γ is normalized by the momentary mean particle velocity. High circulation regions indicate rotating clusters of particles (dots) with a size depicted as circles with the effective radius R_Γ. Parameters read $(m, v_0) = (2.0, 0.4)$ and $t = 500$.

circulation $\Gamma_c(\mathbf{r})$. For a continuous velocity field $\mathbf{v}$ it is defined as the closed line integral

$$\Gamma_c(r) = \oint_{\partial A} \mathbf{v} \cdot d\mathbf{l}. \tag{4.6}$$

If ∂A is the boundary of a surface A, the circulation can be written as flux of the vorticity field $\omega = \nabla \times \mathbf{v}$ via Stokes Theorem, reading $\Gamma_c(\mathbf{r}) = \iint_A \omega \cdot d\mathbf{A}$. Therefore, vorticity as an apparent measure of rotating motion is the circulation per unit area. The concept of circulation is adapted to discrete particle velocities, as schematically drawn in Fig. 4.7 (a). The circulation at a given point $\mathbf{r}$ is computed by averaging the velocity components in circular direction $\hat{\mathbf{e}}_l \perp \mathbf{R}$ from all particles within a radius $R_{\max}$ around this point. Formally, the circulation then reads

$$\Gamma(\mathbf{r}) = \overline{\mathbf{v}_{net}(\mathbf{r}+\mathbf{R}) \cdot \hat{\mathbf{e}}_l}^{R<R_{\max}}. \tag{4.7}$$

The angular unit vector is chosen such that clockwise rotating motion corresponds to a positive circulation. A logically equal definition ($:\Leftrightarrow$) in the continues case would be a weighted average over all radii $R < R_{\max}$ of the circulation Γ_c on a circle ∂A_R

$$\Gamma(\mathbf{r}) :\Leftrightarrow \frac{1}{R_{\max}} \int_0^{R_{\max}} dR \, \frac{1}{2\pi R} \int_{\partial A_R} d\mathbf{l} \cdot \mathbf{v}. \tag{4.8}$$

The reason for introducing the circulation, is to quantify the amount of rotating collective motion in the system. A seemingly natural choice for a measure might be the sample average $\overline{\Gamma^2}$. But then the distinction between systems of some local rotating clusters and systems of several anti-parallel moving translational ones is not given since both might produce similar $\overline{\Gamma^2}$ values due to the averaging. So instead of averaging over the system, only the amount of rare high circulation events is measured which indicate regions of predominant circular motion. This can be seen in Fig. 4.7 (b). The circulation has its maximal/minimal values in the centers of rotating clusters. Therefore the latter are quantified by counting the number N_Γ of local extrema of the circulation. To better distinguish rotational from translational moving clusters the condition $|\Gamma(\mathbf{r})| > \frac{2}{\pi}\overline{v_{net}}(t)$ for possible extrema is used. This threshold is the maximum circulation at the boundary between two anti-parallel moving translational clusters which move with the momentary sample-averaged particle velocity. In order to quantify the typical length scale of rotating clusters, their effective size is measured from the area around cluster positions with $|\Gamma| > 0$. In Fig. 4.7 (b) and Fig. 4.8 this area is depicted as the effective cluster radius R_Γ of circles with these area values. An upper bound for the distance between an area element and the cluster position of $8\,l_0$ is used to avoid overestimation. It is chosen such that it lies slightly above typical values for half the oscillation period of intermediate velocity correlations, like the ones in Fig. 4.6.
In Fig 4.8 an impression for the temporal evolution of N_Γ and the circulation is given. Rotating clusters form and decay in the over- as well as the underdamped regime, but the time scales increase with mass. While for low mass the formation happens quickly after the crystalization, the necessary local alignment is delayed for high masses. At intermediate times, when the number of rotating clusters has almost decayed for low mass systems, it is maximal for high masses and then decays slower. In order to quantify this more precisely the area fraction of rotating clusters in the simulation volume $l_x \cdot l_y$ is measured via the filling factor

$$\eta = \frac{N_\Gamma \, \pi \overline{R_\Gamma^2}}{l_x l_y} \tag{4.9}$$

which is used later on. This number quantifies whether the momentary dynamics is

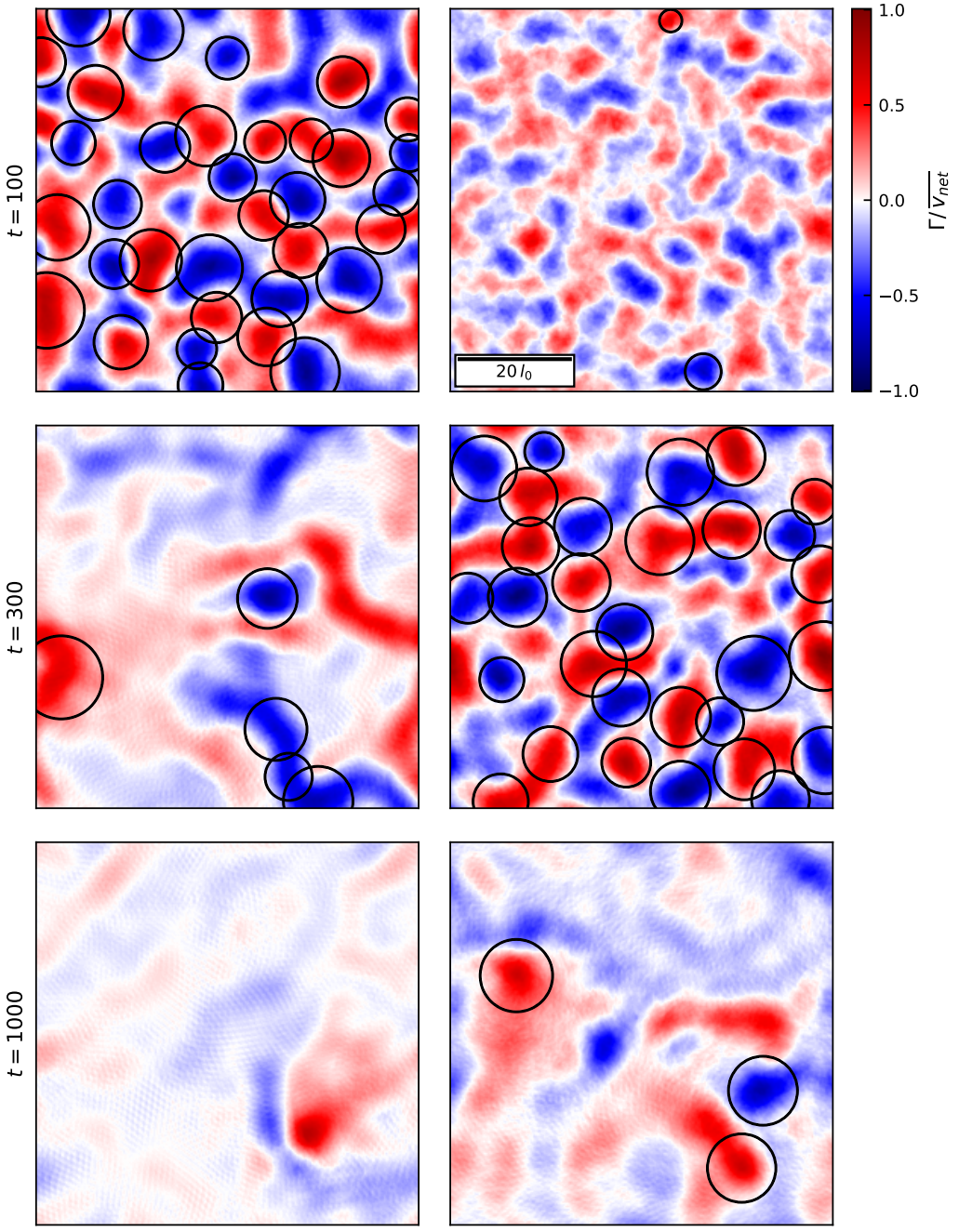

Fig. 4.8.: Circulation in the overdamped ($m = 0.1$, *left*) and underdamped ($m = 2$, *right*) regime at three different times and normalized by the momentary mean velocity in the system. A high circulation value at the order of the momentary averaged particle velocity $\overline{v_{net}}$ indicates predominant circularly motion of particles instead of translational moving clusters. Rotating clusters are depicted as circles with radius R_Γ respectively. The activity is $v_0 = 0.4$.

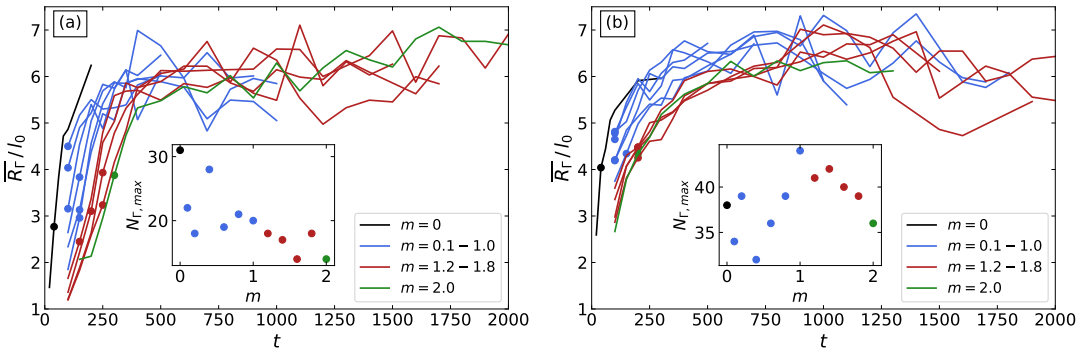

Fig. 4.9.: Sample-averaged rotating cluster radii $\overline{R_\Gamma}$ for (a) $v_0 = 0.35$ and (b) $v_0 = 0.4$. Different mass regimes are color coded. At times where no value is shown no rotating clusters are observed. For both activities, $\overline{R_\Gamma}$ increases and saturates at intermediate times. The markers show the point in time at which the maximum number N_Γ of rotating clusters is observed. Their values are shown in the insets.

governed by rotational motion. A value of $\eta_0 = \pi/4$ corresponds to the extreme case of a frustration free square lattice of equally sized clusters where each is surrounded by four contrary rotating ones.

Similar to the formation of translational moving clusters, rotating ones form and grow due to local alignment of orientations. It can be seen in Fig. 4.9 that this expresses as a continues increase of R_Γ for short times. The values for $m = 0$ are obtained from the overdamped limit model in Eq. (2.26), analyzed with the migration method. The shown values of R_Γ for $m = 2$ can be connected to the corresponding velocity correlations Fig. 4.6. In the above described intuition of separating C_v into contributions from translational and rotational clusters it was already noted that for $t = 300$ mainly the oscillating part of rotating clusters is observed which therefore dominates. And indeed, in Fig. 4.8 many rotating clusters are present at that time. Half the period of the C_v oscillation, meaning the distance between the first minima and following maxima, can be read off approximately as $8\,l_0$ ($v_0 = 0.35$) and $10\,l_0$ ($v_0 = 0.4$). These values are also found for the cluster diameter $2\,\overline{R_\Gamma}$ at this time, which highlights rotating clusters as the pyhsical origin of the oscillating velocity correlations. Further, it can also be seen that the mass parameter delays the growth process of rotating clusters. This is due to the fact that particles need to align their orientations locally when started in an isotropic state, before any larger clusters can form. In the overdamped limit the corresponding change of actual velocity happens instantly, while it is delayed when

inertia is incorporated. As observed in the simulations, this destabilizes the formation of small collectively moving clusters for high mass. And consequently, the growth of the effective cluster radii R_Γ happens delayed in time when inertia is increased. For both explored activities and all masses the cluster radius saturates during intermediate times between five and seven particle length scales l_0. This suggests that a preferred cluster radius exists which might be more influenced by the local alignment strength than mass or activity. This dependence is however not investigated further here. Also shown is the maximum number of observed rotating clusters which is always found during the initial formation process. Their values are discussed later on.

Collective Time Scales. Many of the shown curves in Fig. 4.9 end at some point in time, indicating that no rotating cluster is observed since then, meaning $N_\Gamma = 0$. Especially for $v_0 = 0.35$, but also for $v_0 = 0.4$, only clusters in the underdamped regime have still not decayed after long times. This raises the question of how many rotating clusters are observed in dependence of mass and activity over time. Or in other words, how large is the fraction of circularly moving particles over time. In Fig. 4.10, this is quantified with the temporal evolution of η, which shows qualitatively the same curse for all parameters. An initial rise, reflecting the formation and growth of rotating clusters over a time τ_f, followed by a decline during which the clusters decay again over the time τ_d. Motivated by these qualitative systematics, a phenomenological expression for the filling factor is suggested in order to explain its parameter dependence. τ_f and τ_d are treated as exponential time scales, which leads to the expression

$$\eta(t) = \eta_0 \left(1 - e^{-t/\tau_f}\right) e^{-t/\tau_d}. \tag{4.10}$$

This function is used to extract the mass and activity dependent formation and decay time scales. For these fits, the value $\eta_0 = \pi/4$ stays fixed and a variable time offset is used to account for the varying onsets of crystallization from the supercooled liquid. In Fig. 4.10 it becomes apparent that Eq. 4.10 suffices to describe the system for all explored parameters. The insets show that for $v_0 = 0.35$ the time scales τ_f and τ_d increase linearly with inertia. For $v_0 = 0.4$ the formation of circulating clusters happens comparably faster in the underdamped regime, leading to smaller τ_f times which are barely influenced by inertia. The decay time differs from a linear mass dependence by first increasing in the overdamped regime and then saturating in the underdamped regime. The parameter dependent formation and decay times represent the main result of this

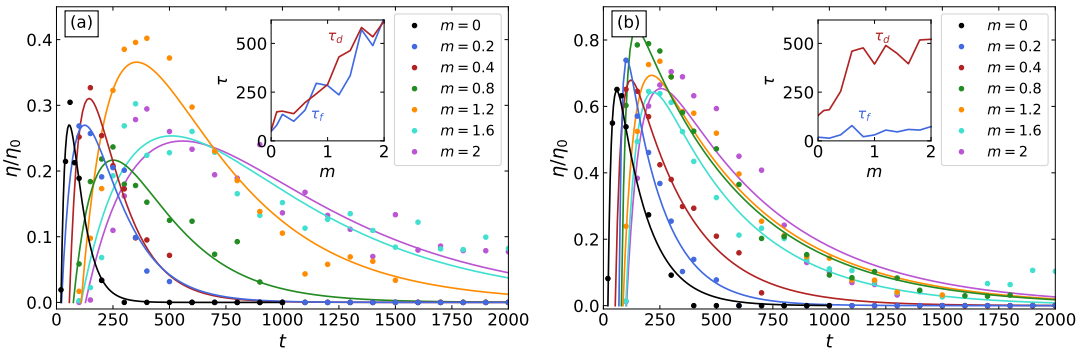

Fig. 4.10.: Rotating cluster filling factor η for (a) $v_0 = 0.35$ and (b) $v_0 = 0.4$. Large values indicate predominant circular motion in the system. The temporal evolution is of η is governed by initial formation and followed decay of rotating clusters. The insets show that the time scales of both processes depend on mass and activity. The same data as in Fig. 4.9 is used.

investigation since they summarize the consequences of introducing inertia on the collective dynamics. In order to physically explain their found behaviour, an idealized conception for the formation and break-up mechanism of rotating clusters is suggested and compared to the results in the following.

As described earlier, smaller collectively moving clusters form after the initialization from isotropic initial conditions. At the boundary between two contrarily moving small clusters, particles may switch from one of these common migration directions to the other and therefore have to rotate their orientation. The corresponding change in motion happens instantly in the overdamped limit. As schematically drawn in Fig. 4.11 this exchange of particles drives the formation of a circulating cluster, which then grows due to the preferred local alignment of orientations. Such a situation can be seen in Fig. 4.2 (a). On the other hand, when inertia is relevant the actual motion of particles does not follow a sudden change in orientation immediately. So instead of joining the contrarily moving clusters, a particle might reorient back to its current one. Therefore, the probability of initializing a circulating cluster decreases with mass and its growth process is delayed to later times. This explains the decreasing maximum number of N_Γ and the increase of τ_f with m for $v_0 = 0.35$. However, an increase in active drive counteracts this tendency by increasing the acceleration in the direction of the orientation. Judging from the comparably high maximum N_Γ and low τ_f values for $v_0 = 0.4$, this activity suffices to considerably increase the probability of initiating a rotating cluster.

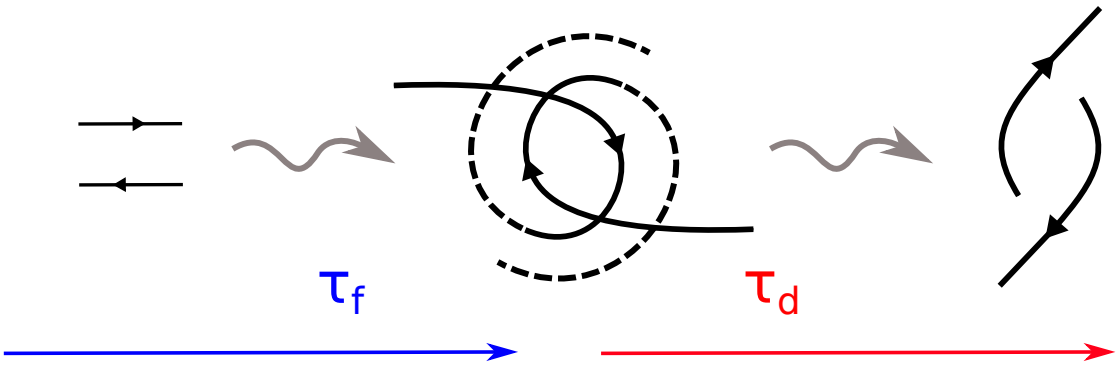

Fig. 4.11.: Idealized mechanism for the formation and break-up of rotating clusters. The arrows depict local collective motion of groups of particles. First, small translational clusters build in the system due to local alignment of orientations. Occasionally they bypass each other contrarily. At the boundary, particles may switch between the two common migration directions by rotating their orientation. If particles from both clusters are trying this, they try to align with each other too. But during this they move further past each other, so they have to rotate their orientation even further. This can lead some particles to circulate around the midpoint between them, constantly trying to rotate their orientation into the direction of their anti parallel moving neighbour. Around them over particles can align to one of them, driving the formation of a growing rotational cluster whose radius saturates when equally many particles enter and leave the rotating region. These processes happen during the formation time τ_f. The PFC interaction favours a hexagonal structure of density peaks which is not given in rotating clusters. Therefore, after the decay time τ_d the cluster breaks up again into translational moving ones with hexagonal symmetry.

Once a rotational cluster has formed and grown, its effective radius R_Γ saturates at a constant value. As depicted in Fig. 4.11 during the following intermediate time scale, particles leaving the cluster are substituted with incoming ones from translationally moving clusters. The reader is encouraged to compare this conception with the attached video *ActiveCrystal.mp4* (App. B). Such translational clusters of particles around a rotational cluster can be seen by eye at some points. However, after some time the systems preference for a hexagonal particle structure and uniform orientation will break-up rotating structures back into translational ones with hexagonal symmetry. At least two scenarios are imaginable how this could happen. One is that more and more particles at the edge of rotating clusters align to surrounding translational ones, which would lead to a steadily decreasing cluster radius until the rotational cluster has dissolved. The second is that the rotational cluster more abruptly breaks up into several translational ones, which would mean that high R_Γ values can still be observed shortly before the rotational cluster is not detected as such any more. Judging from Fig. 4.9 the second scenario is more likely, since the shown radii R_Γ do not decrease to smaller values before the curves end, which is when the last rotational cluster has disappeared. For increasing inertia, the PFC acceleration is lowered and therefore needs longer to break-up rotating clusters into translationally moving ones. This explains the with m increasing decay times τ_d observed for both activities. A higher activity counteracts this break-up into contrarily moving clusters with the same mechanism as in the formation process. Therefore, the τ_d values are higher for $v_0 = 0.4$ in the overdamped regime. But it is noted that τ_d saturates in the underdamped regime for this higher activity. This is clarified with the high filling factor, with peak values in the range of η_0. The high maximum of η is due to many rotating clusters which still have not reached their maximum radius at that time, as can be seen from Fig. 4.9 and Fig. 4.10. The competition for space needed for their growth causes some clusters to break-up, which decreases η already before the average cluster radius saturates. This explains the upper bound for τ_d. For lower activity this is not observed. Here, a lower number of rotating clusters can grow to its maximum size, which then corresponds to the maximum of η.

Lastly, it is noted that the variation of the maximum η values with m is most probably due to statistical uncertainty. This is exemplary demonstrated by running four simulations with the same parameters $(m, v_0) = (0.8, 0.35)$. The resulting fit maxima vary with other 10% relative to their mean $\eta_{max}/\eta_0 = 0.29 \pm 0.03$.

Discussion

Dynamics. The above used distinction of translational and rotational clusters and the suggested formation and break-up mechanism for the latter are able to explain the found time scales tor the collective dynamics qualitatively. What became clear is that introducing inertia into the system slows down the relaxation to the globally ordered state. However, this delay does not trivially scale with the dimensionless damping time $\gamma^{-1} = m$ which only describes the time scale of individual particle velocity relaxation. Also a higher collective time scale $\propto \gamma^{-1}$ is not found in quantities like the time dependent velocity correlation length (not explicitly shown). Instead the extracted formation and decay time scales describe the temporal evolution appropriately.
Additional insight into the cluster dynamics might be possible with other model approaches. In contrast to the current continuum model, particle based simulations can trace individual trajectories for longer times and are therefore also able to directly observe cluster dynamics by categorizing locally aligned particle clusters into translational and rotational ones depending on whether their trajectories follow straight lines or circular orbits. It might be interesting to test if a rotational cluster indeed breaks up abruptly into translational ones, which is not directly observed in this work, but inferred from the measured cluster radii. Particle based simulations with interaction rules comparable to the ones used here also find transient circulating particle clusters before a global migration direction has established [53]. However, these simulations are done at lower particle densities, well below a near crystalline packing. In systems of high densities and/or soft interaction potentials, larger time scales become technically inaccessible for particle simulations. This highlights the advantage of the used PFC continuum approach.
It is noted that the convective term $(\mathbf{v} \cdot \nabla)\,\mathbf{v}$ present in the model can be neglected without changing the found results. This is exemplary tested by measuring the formation and decay time without the convective term at $(m, v_0 = 2, 0.4)$. The found values $\tau_f = 54, \tau_d = 580$ agree with the original results.

Finite Size Effects. Active systems are known to adapt their collective dynamics depending on the boundary conditions. Especially convex confinements, as typical experimental setups of polar rods are considered [1, 33, 34]. There, rotational swarming can be observed due to interactions with the confining wall. Also the overdamped active crystal model is known to change its dynamics due to the frustrated crystal geometry in a geometrical confinement [54]. All shown results for the present underdamped active

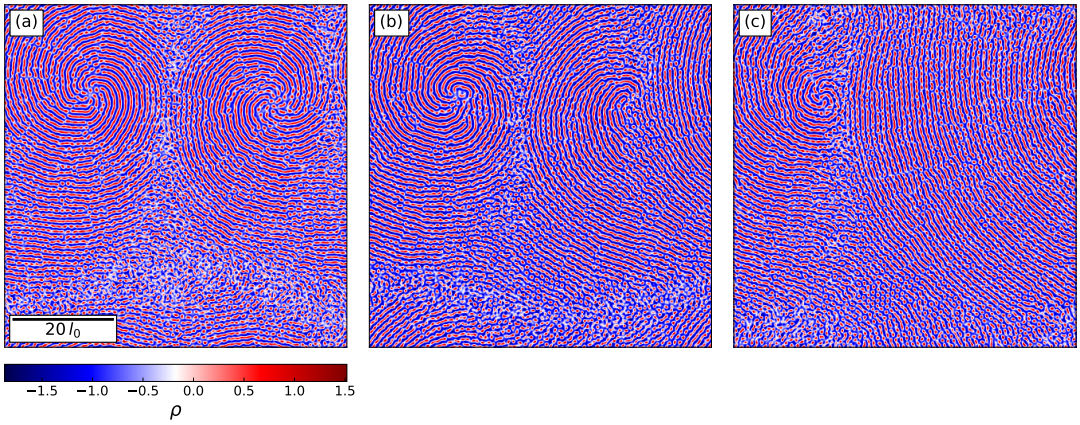

Fig. 4.12.: Density field of the full simulation box at (a) $t = 3000$, (b) $t = 4000$ and (c) $t = 5000$. At high active drive, large scale transient vortices form which self-interact over the periodic boundaries, due to their size. Such rotating clusters might be stabilized in a circular confinement. Parameters read $(m, v_0) = (1.8, 0.42)$.

crystal model are obtained in the context of periodic boundary conditions. However, when the active drive v_0 is increased further as considered so far, large transient spiraling structures can be observed. Like shown in Fig. 4.12, the hole simulation box can be spanned by one of them if the others have decayed. A higher mass strongly increases the lifetime of such a global spiraling state. Different to the finite sized rotating clusters at lower activities, this outward spiraling structure becomes large enough to self-interact over the periodic boundaries and therefore decays. It is suggested that such structures might be stabilized within an e.g. circular confinement. Therefore the present model might proof as a promising approach to investigate the role of inertia for the large scale collective dynamics in confined geometries.

4.3. Extensions of the Model

So far advection of the orientation field is neglected in the discussed active crystal model. Its influence on the dynamics is now described. The dynamical equation for $\mathbf{P}$ in Eq. (2.25) is altered by including the advective term $(\mathbf{v}\cdot\nabla)\,\mathbf{P}$. For clarity the resulting set of dimensionless equations is stated here, which reads

$$\begin{aligned}
\frac{\partial\rho}{\partial t} &= -\,|\overline{\rho}|\;\nabla\cdot\mathbf{v}\\
\frac{\partial\mathbf{v}}{\partial t}+(\mathbf{v}\cdot\nabla)\,\mathbf{v} &= \frac{1}{m}\left(-\mathbf{v}-\nabla\left[\left(\epsilon+\left(1+\nabla^2\right)^2\right)\rho+\rho^3\right]+v_0\,\mathbf{P}\right)\\
\frac{\partial\mathbf{P}}{\partial t}+(\mathbf{v}\cdot\nabla)\,\mathbf{P} &= \left(C_1\,\nabla^2-D_R\right)\mathbf{P}-\frac{v_0}{|\overline{\rho}|}\,\nabla\rho.
\end{aligned}\tag{4.11}$$

From the density field in Fig. 4.13 it becomes apparent that the system's behaviour has changes qualitatively in this extended model. In the overdamped regime, a self-separation into constant high and low density clusters is observed with hexagonal density peak structures in between. The latter form and dissolve continually at their boundary to a constant density region while the peaks are also mobile. These dynamics are explained with the flow field around density peaks, exemplary shown in Fig. 4.13 (b). In the active crystal model without $\mathbf{P}$ advection, density peaks self-propel in the traveling crystal state since the orientation field causes a net flow at the density peak maximum, as shown in Fig. 4.4. Including advection of $\mathbf{P}$ changes this mechanism, since then the arising velocity field advects the orientation field away from the peak maximum. In the resulting steady state in Fig. 4.13 (c) high orientation amplitudes do no longer coincide with density peak maxima. The flow induced by this orientation field around peaks then transports density away from one peak to another, see Fig. 4.13 (b). In a bulk of hexagonally ordered density peaks this means that every peak accumulates density at one side while it looses density at the other, effectively causing every peak maxima to move in opposite direction of the flow field. Consequently, the peaks shown in Fig. 4.13 (b) are observed to move in the upper right direction, since the flow field points to the lower left.
At the boundary of a crystalline structure the described flow field can point towards the constant density neighbourhood and cause a fluctuation there which drives the formation of new peaks due to the PFC instability. If at a boundary region new peaks arise quicker than they move away, the crystalline structure grows into the constant density region. On the other hand, if the flow field points towards the crystalline region, a peak at

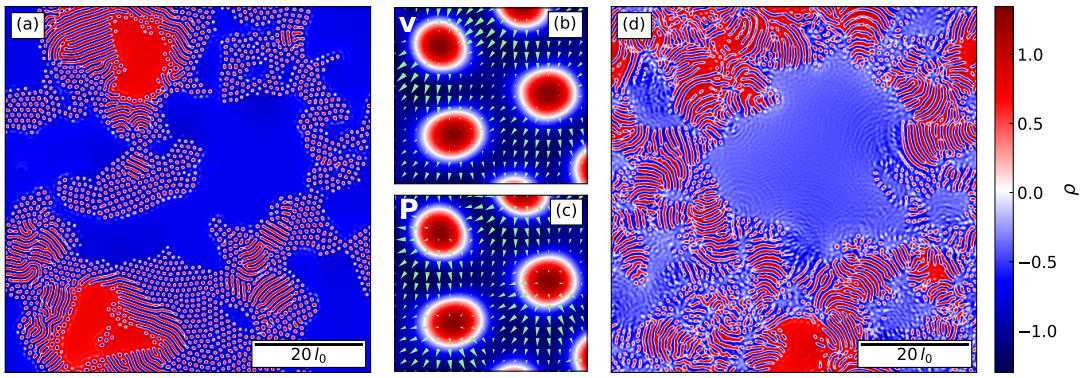

Fig. 4.13.: (a): Snapshot of the density field for the extended active crystal model in Eq. (4.11) at $m = 0.1$. The system decomposes into constant high and low density regions with hexagonal crystals of density peaks in between. The latter continually form and dissolve at their boundary to constant density regions. This happens due to the flow field around density peaks (b) induced by the orientation field (c). (d): For higher mass $m = 2$, the clear crystal structure dissolves in a stripe pattern and the decomposition is less distinct. For both masses is $v_0 = 0.4$ and $t = 1000$.

the boundary transports density into the crystal bulk while not regaining the lost amount from the constant density region until a new peak forms there out of a density fluctuation. Similar to the situation with the oppositely directed flow field, the crystal structure then grows or shrinks, depending on whether a new peak forms at the boundary before the current lost its density due to the flow into the crystal bulk. This dynamical formation and liquefaction of density peaks can be observed in the attached movie *ActiveCrystalAdvection.mp4* which is described in App. B. Also visible there, is the growth of the constant high density regions in Fig. 4.13. Such regions evolve where several crystalline regions with different orientations of their flow field transport density into the same volume. The accumulation of density saturates at a constant value since the cubic nonlinearity of the PFC interaction gives an effective upper bound for the absolute value of the local density.

A reason for the stability of the constant density regions is the isotropic orientation there. Since no local alignment evolves in the homogeneous density region, also no net flux is induced which could cause the density field to disolve. The described characteristics of an separation into regions with different density are reminiscent to motility induced phase separation (MIPS), commonly found in active systems [55]. In this context, the high density regions in the current model correspond to close packings of particles which block each others motion leading to the found isotropic mean orientation. The low den-

sity regions then correspond to a gas like state where particles are on average too far apart to interact or build collective structures. Therefore the observed mean orientation and velocity are also isotropic there. Only in regions of intermediate density, local alignment interactions lead to collective structures, which express in the present model as moving density peak crystals. A recent investigation of underdamped active particles shows that the formation of MIPS is inhibited for sufficiently large particle mass [56]. Also in the underdamped regime of the present model the clear separation into high and low density regions seems less distinct when comparing Fig. 4.13 (a) and (d), which is however not further investigated here. The general underdamped continuum model introduced in Eq. (2.20) with appropriately chosen interaction rules might serve as a useful tool to study the role of inertia in the formation of MIPS.
Due to the different propulsion mechanism, a simple interpretation of density peaks as particles is no longer adequate in the described extended model. An attempt to regain the picture of particles within systems incorporating both convective terms, is to weight the active drive v_0 in the velocity equation (4.11) with the density field, in order to induce an active velocity only where a particle is located, namely at density peaks. Two possibilities for the density dependence of v_0 are considered, which read

$$\begin{aligned} v_0(\rho) &= v_0 \, \frac{\rho - \overline{\rho}}{|\overline{\rho}|} \\ v_0(\rho) &= v_0 \, \frac{|\rho| - \rho_{min}}{\rho_{max} - \rho_{min}} \end{aligned} \tag{4.12}$$

where ρ_{max} and ρ_{min} are the minimum and maximum density value produced from the PFC functional. However, for both modifications no qualitative difference to the results in Fig. 4.13 are observed.

5. PFC Alignment Model

In the following, results for the PFC alignment model introduced in Ch. 2.3 are presented and discussed. First, the observed steady states in the overdamped limit are described and compared with literature in order to serve as a reference for the discussion of the corresponding underdamped model. It is found that introducing inertia into the system can destabilize the force balance in otherwise steady states, resulting in a self-sustained non-steady state, referred to as turbulent. Further, a global collective motion state, also not present in the overdamped limit, is observed.
The mean density in all simulations is set to $\overline{\rho} = 1.0$.

5.1. Overdamped Limit

For clarity the dimensionless overdamped limit equations of the PFC alignment model introduced in Eq. (2.33) are stated here again:

$$\begin{aligned} \frac{\partial \rho}{\partial t} &= \frac{1}{2}\nabla^2\rho^2 - v_0\,\nabla\cdot(\rho\,\mathbf{P}) \\ \frac{\partial \mathbf{P}}{\partial t} &= \left(1-|\mathbf{P}|^2\right)\mathbf{P} - \lambda\left(1+\nabla^2\right)^2\ \mathbf{P}. \end{aligned} \tag{5.1}$$

The interaction of particle orientations consists of two contributions. The first term in the dynamical equation of $\mathbf{P}$ favours local alignment while the second one prefers a periodic structure of orientations on the length scale $l_0 = 2\pi$, corresponding to the PFC wave number $q_0 = 2\pi/l_0$ which is set to one in the used rescaling. The strength of the latter interaction is controlled by the parameter λ. By varying its value, different steady states are found, as can be seen in Fig. 5.1. The shown velocity fields are computed via the current in the continuity equation $\dot{\rho} = \nabla\cdot\mathbf{j}$, reading

$$\mathbf{v} = \frac{\mathbf{j}}{\rho} = -\nabla\rho + v_0\,\mathbf{P}. \tag{5.2}$$

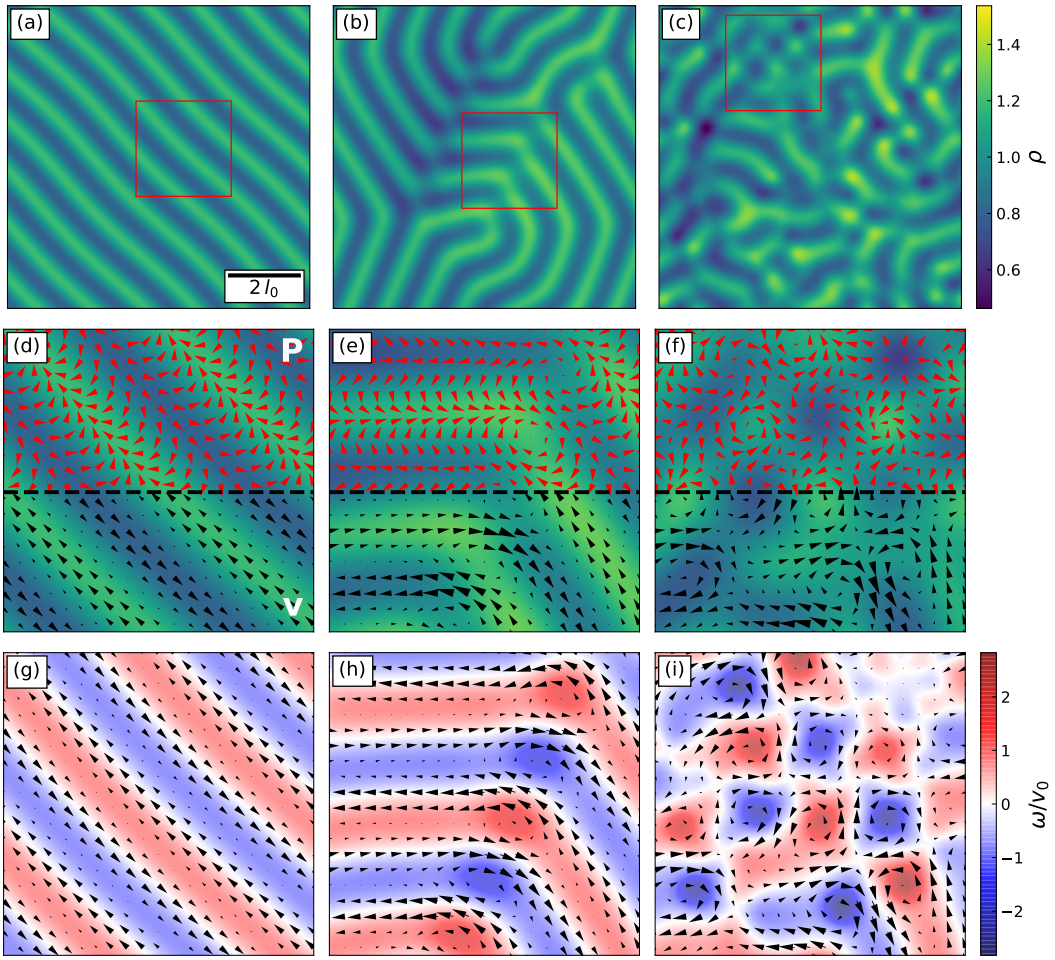

Fig. 5.1.: Snapshots of different states for varying anti-alignment strength, ordered by columns: left $\lambda = 3$, middle $\lambda = 0.5$, right $\lambda = 0.03$. (a-c) Particle density over the hole simulation volume. The boxed region is magnified in (d-f) and (h-j) respectively. The second row shows the magnified density field, in one half overlaid with the orientation field (red) and in the other half with the velocity field (black). The third row shows the velocity field and its vorticity $\omega = (\nabla \times \mathbf{v}) \cdot \hat{\mathbf{e}}_z$. At high anti-alignment strengths $\lambda = 3$ the system is likely to reach a global laning state of periodically high and low density bands, along which particles propel in lanes (first column). Due to the preferred anti-alignment of orientations, particles in neighbouring lanes move in opposite directions. The velocity all lanes is equally high, causing a net particle current in the movement direction within the high density bands. The vorticity of the velocity field only has low values between anti-parallel oriented lanes. By lowering λ vortical defect boundaries in the orientation field are observed between laning domains (second column). In the vortex state for very low λ vortical motion arranged in local square lattices is observed, driven by the orientaion field (third column). Simulation time is $t = 5000$ and $v_0 = 0.2$ for all systems.

For high λ orientations vary periodically, which minimizes the corresponding free energy functional term belonging to this parameter. Physically, λ is therefore interpreted as an anti-alignment strength of particles at distance $l_0/2$. From Fig. 5.1 (a,d) it can be seen that the resulting regular orientation field accumulates density in bands with the periodicity l_0. This process is balanced by the compressibility of the system, counter acting along the arising density gradients. In the shown steady state the density and orientation fields in dimensional form are described by

$$\begin{aligned} \rho(x) &= \rho_0 \, \cos(q_0 \, x) + \overline{\rho} \\ P_x(x) &= \sqrt{\frac{a}{\beta}} \, \sin(q_0 \, x) \\ P_y(x) &= -\sqrt{\frac{a}{\beta}} \, \cos(q_0 \, x) \end{aligned} \tag{5.3}$$

in a reference frame along the density gradient. The amplitude of the density variation ρ_0, is predicted from inserting these expressions into Eq. (5.2). In the steady state $v_x = 0$, this yields

$$\rho_0 = \sqrt{\frac{a}{\beta}} \, \frac{v_0 \, \alpha}{q_0 \, c} \tag{5.4}$$

or $\rho_0 = v_0$ in dimensionless form. This density amplitude is in accordance with numerically found global stripe patterns, like Fig. 5.1 (a). Along the maxima and minima of the density bands the local alignment of orientations induces a particle flux, whereas between the lanes the self-propulsion in density gradient direction is counter acted from the compressible force. The particles are at rest there, which leads to the velocity pattern in Fig. 5.1 (d,g). In a physical context this is refered to as a laning state [35, 37, 38, 57]. Due to the preferred anti-alignment particles in neighbouring high and low density lanes propel in opposite directions. The self-propulsion velocity v_0 is chosen independent of the local density. Therefore, particles in high and low density lanes move with this equal velocity and a net current in the direction of movement within high density lanes can be observed. By averaging the current over two neighbouring lanes, its value is computed with Eqs. (5.2), (5.3) and (5.4) to

$$\overline{j} = \frac{1}{l_0} \int_0^{l_0} dx \; v_y \, \rho = \frac{v_0^2 \, \alpha \, a}{2 \, c \, \beta} \tag{5.5}$$

or $\overline{j} = v_0^2/2$ in dimensionless form. In the extreme case $v_0 = \rho_0 = \overline{\rho}$, all particles might accumulate in the high density bands and move in the same direction, thereby maximizing the current, which is however not explicitly tested. Such unidirectional laning states are observed in particle simulations with orientational alignment. There, the maximum distance of local alignment coincides with the resulting lane distance [35]. In this reference the formation of lanes is explained as an overreaction of the alignment interaction. This differs from the formation mechanism of lanes observed here, since alignment of particles happens only locally and an anti-alignment rule dominates at further distances, which determines the lane spacing.
When the anti-alignment strength λ is lowered, the orientation field becomes more likely to locally form vortices with length scale l_0, as in Fig. 5.1 middle column. Seeing the combined alignment and anti-alignment orientational interaction as the derivative of a vectorial PFC functional, the increasing occourence of vortices between laning domains can be seen as a transition from the stripe to the crystal state. The difference to a one component PFC interaction, as for the density field in the active crystal model, is the coupling of the two vector components of $\mathbf{P}$. So, instead of a clear transition from a laning (stripe) state to a regular lattice of vortices (crystal) state, it is observed in Fig. 5.1 (b,e) that the system typically is stuck in metastable states of local laning domains separated by defects in the form of vortices in the orientation field. Those defects increase the free energy of the λ term relative to the global laning state, suggesting that the anti-parallel alignment is less given there. Over longer simulation times, some defects might heal out and for small system sizes the global laning state can be reached. However, in larger systems this does practically not happen. Instead, local vortex defects persist between laning domains which span most of the simulated volume for intermediate λ values. In this parameter regime it is observed that the system accumulates density near vortex defects which lie between laning domains where particles in the high density lanes are orientated towards those defects. The mechanism for this works as follows: Large laning domains can span most of the simulation box, as shown in Fig. 5.1 (e) or for a larger simulation volume in Fig. 5.2. In the respectively shown magnified regions, a boundary of vortex defects in the orientation field between two laning domains is present. Particles in the high density lanes move towards the defects, and partially circulate there in the vortical defects of the orientation field and therefore increases the local density. Other particles instead leave the boundary region over the low density lanes. Therefore, the density near the boundary is also increased in the low density lanes. Particles in high density lanes then have to move against a gradient, while the oppositely directed particles in the low density bands move in downward direction of the gradient.

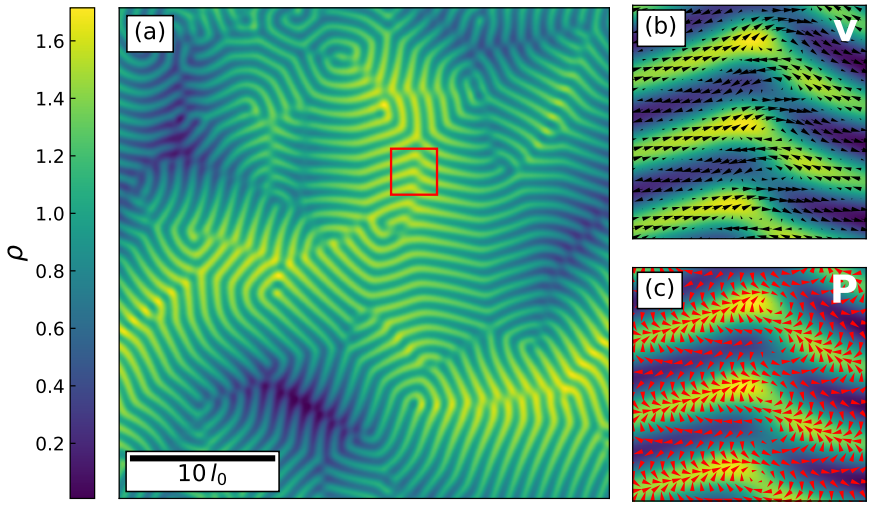

Fig. 5.2.: (a): Density field of a system with intermediate anti-alignment strength $\lambda = 1$ in a larger simulation box. The system self-separates over time in high and low density regions. (b,c): Magnification of the boxed region with velocity and orientation field, respectively. In this metastable state particle density accumulates at defect boundaries between two laning domains, where particles in the high density bands move towards the boundary.

Consequently, particles moving towards the domain boundary are decelerated and particles leaving the boundary are accelerated from the compressibility. In the final steady state, the density gradient along both lane directions is high enough to balance the currents which enter the defect region with those leaving it, resulting in a static density field. In larger simulation volumes this leads to a large scale self-separation of the system towards the described boundary type, as illustrated in Fig. (5.2).
When λ is further lowered to small values the vortex state is reached, in which the number of vortices in the orientation field steadily increases until clear laning domains are not observed any more. In the steady state, typically no large scale self-separation within the density field is observed as demonstrated in Fig. 5.1 (c). Instead the found density pattern varies locally, depending on the metastable state of the orientation field in that region. Small laning structures cause larger density variations with the same self-separation mechanism as in the global laning state. What is increasingly found, are several vortices in the orientation field which arrange next to each other and result in local lattices of alternating clockwise and anti-clockwise motion, shown in Fig. 5.1 (c,f,i). Only square lattices are observed, different to the hexagonal lattice symmetry arising

for one component PFC functionals. This difference arises since the PFC form of the orientation interactions couples both components of $\mathbf{P}$. The resulting vortices in the orientations field are frustration free only in a square lattice, where each rotating vortex is surrounded solely by vortices with different rotation directions. This preferred structure would not be given in a triangular array of vortices. It is further noted that the local square lattice is typically distorted by its surrounding. Therefore, inward and outward spiraling vortices in the orientation field are observed instead of perfect circular ones. Inward spiraling orientations accumulate density, while outward spiraling ones spread density. In the steady state this results in the observed density variations between contrary rotating vortices, which are balanced by the compressibility, so that a square lattice of perfectly circular vortices in the velocity field is observed in Fig 5.1 (i).

5.2. Non-equilibrium States in the Underdamped Model

The states found in the overdamped limit now serve as a reference in order to discuss the underdamped PFC alignment model. The dynamical equations of the latter, introduced in Eq. (2.32), are stated here again for clarity:

$$\begin{aligned} \frac{\partial \rho}{\partial t} &= -\nabla \cdot (\rho\, \mathbf{v}) \\ \frac{\partial \mathbf{v}}{\partial t} + (\mathbf{v} \cdot \nabla)\, \mathbf{v} &= \frac{1}{m} \left(-\mathbf{v} - \nabla \rho + v_0\, \mathbf{P}\right) \\ \frac{\partial \mathbf{P}}{\partial t} + (\mathbf{v} \cdot \nabla)\, \mathbf{P} &= (1 - |\mathbf{P}|^2)\, \mathbf{P} - \lambda \left(1 + \nabla^2\right)^2\, \mathbf{P}. \end{aligned} \tag{5.6}$$

It is reminded that the preferred wave number q_0 in the PFC interaction is set to one in this rescaling, like in the overdamped limit model. The corresponding preferred length scale in real space is denoted as $l_0 = 2\pi/q_0$.

Results

In the following, the state diagram is explored along two lines in parameter space, once for varying anti-alignment strength λ and also for varying activity v_0. First, parameter regimes where the system's behaviour changes qualitatively, are identified via spontaneous changes in variables for density fluctuations and velocity alignment. Second, the found non-equilibrium states laning, turbulence and collective motion are discussed separately. And third, the role of the particle mass on the turbulent state is investigated. The fluctuations in the density field are characterized via the space-averaged variance

$$\Delta\rho^2 = \overline{\rho^2} - \overline{\rho}^2. \tag{5.7}$$

For global laning structures in the overdamped limit the variance is given from the density profile in Eq. (5.3), leading to the dimensionless value $\Delta\rho_0 = v_0/\sqrt{2}$. Especially in the later discussed turbulent regime, the system's order parameter fields are strongly fluctuating over time, which expresses in a corresponding fluctuation of $\Delta\rho$. Because of this it is more instructive to also introduce the ensemble averaged density fluctuation

$\langle \Delta\rho \rangle$, meaning the average over many realizations of the same system with different initial conditions in order to extract statistically relevant values. Here, the assumption of ergodicity is made, meaning that the phase space is sufficiently explored by the system and therefore the ensemble average of an observable over many system realizations coincides with the time average over one sample. Then, the density fluctuations can be measured with the spatio-temporal average

$$\langle \Delta\rho \rangle = \frac{1}{T} \int_{t_0}^{t_0+T} dt \; \Delta\rho(t) \tag{5.8}$$

over a time interval $T = 8000$ with the start time $t_0 = 12000$ after which relaxation from the initial conditions is finished. In the following, the mean value $\langle \Delta\rho \rangle$ is used to quantify density fluctuations in space, while the corresponding variance is used as a measure for temporal fluctuations.
Further, the alignment within the velocity field is quantified by measuring the space averaged polar orientational order of the normalized velocity field

$$p_v = \left\| \overline{\mathbf{v} / \|\mathbf{v}\|} \right\| \tag{5.9}$$

where $\|\cdot\|$ denotes the vector norm. A value near one indicates global orientational order of the velocity field, while zero indicates the absence of global ordering.
The average density fluctuations $\langle \Delta\rho \rangle$ and the velocity orientational order p_v are measured for different λ at a high activity $v_0 = 0.2$. From the shown results in Fig. 5.3 (a,c) three qualitatively different states can be distinguished. They are described later in detail and examples are shown Fig. 5.4. First, for high anti-alignment strengths, the average density fluctuations are close to $\Delta\rho_0$ and their variance is negligible. The system shows no global ordering of velocities. In this regime, the same laning state as in the overdamped limit is found. Second, near the critical value $\lambda = 0.1$, the mean density fluctuations and their temporal variance suddenly increase which is accompanied by an onset of global orientational velocity ordering in p_v. This state is referred to as turbulent, due to the reminiscence of the observed spatio-temporal fluctuations to classical turbulence in passive systems. And third, in the low λ regime, the mean density fluctuations decrease again relative to the turbulent state and even below the characteristic value $\Delta\rho_0$ of the laning state. The temporal variance stays high. In this regime global ordering of velocities is observed with p_v values near one, leading to the identification of

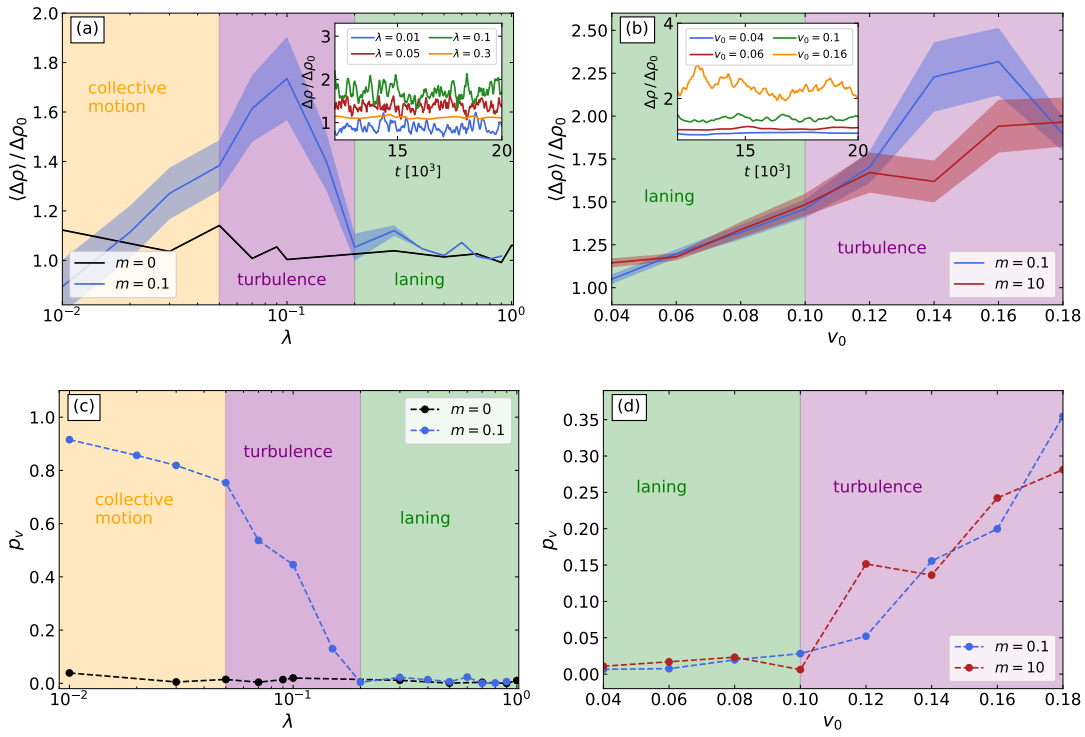

Fig. 5.3.: Cuts through the parameter space along λ at $v_0 = 0.2$ (a,c) and along v_0 at $\lambda = 0.1$ (b,c). The temporal average of density fluctuations $\langle\Delta\rho\rangle$ with its variance and polar velocity order p_v distinguish qualitatively different states in the underdamped model, indicated by background color: laning (green), turbulence (purple) and collective motion (orange). The insets in (a,b) illustrate exemplary time courses of $\Delta\rho$ for $m = 0.1$. (a,c): By lowering λ, a transition from laning to collective motion with a turbulent transition state is observed in the underdamped model (blue curves). Coming from the laning state, spatio-temporal fluctuations increase abruptly in the turbulent state and a onset of global velocity ordering is observed. During the transition to collective motion spatial density fluctuations decrease again and global velocity order $p_v \approx 1$ is found. For comparison $\langle\Delta\rho\rangle$ and p_v, measured in the overdamped model Eq. (5.1) are shown (black curves), where a steady state with local vortex lattices is found for low λ instead of turbulence and collective motion. Nether an increase in spatio-temporal density fluctuations, nor a onset of collective motion are observed there. (b,c): Lowering the activity in the turbulent state $\lambda = 0.1$ results again in laning, marked by low density fluctuations and absent global velocity ordering. For over- and underdamped mass parameter, $m = 0.1$ and $m = 10$ respectively, the same states are identified.

this state as collective motion.
The turbulent transition regime between laning and collective motion, is further explored by lowering the active drive v_0 at fixed $\lambda = 0.1$. Again, the average density fluctuations $\langle \Delta\rho \rangle$ and the velocity orientational order p_v are measured. The shown results in Fig. 5.3 (b,d) again indicate a transition between qualitatively different states. The already found turbulent state persists down to lower activities as long as high spatio-temporal density fluctuations and non-zero velocity ordering p_v are observed. If activity is low enough, density fluctuations decrease to $\Delta\rho_0$ and velocity ordering is completely absent. Here, the laning state is again observed.
The above listed states are discussed in the following.

Laning. For high λ values the laning state, described within the overdamped model, is also found in the underdamped model. The steady state density bands yield the temporally non-varying values $\Delta\rho_0$ for the average density fluctuations (Fig. 5.3 (a)). The characteristic net particle current along lanes of alternating density and orientation is observed as discussed earlier (Eq. (5.5)). Since particles in high and low density lanes move equally fast in opposite directions, global ordering of velocity orientations is absent, $p_v = 0$ (Fig. 5.3 (b)). What changes in the underdamped model is the regime where self-separation, as in Fig. 5.2, happens. While the necessary vortical defects in the orientation field are still found for higher anti-alignment $\lambda \gtrsim 1$, they are absent when λ is lowered, different to the overdamped limit. An example of this is shown in Fig. 5.4 (a,d,g). This is explained with the advection of orientation. A local vortex in the orientation field induces a corresponding vortical flux. Due to their inertia, particles radially leave the vortex, which then gets distorted due to the advected orientation. The anti-alignment interaction counteracts this distortion, similar to an centripetal force which holds objects on circular orbits. Consequently, if its strength is lowered enough, the formation of vortices in the orientation field is inhibited. In the steady state the grain boundaries between different laning domains are then resolved by branching and linkage of lanes with equivalent orientation at the boundary (Fig. 5.4 (d)). Therefore, advection is actually beneficial for the formation of a global laning state at intermediate anti-alignment strengths since it heals out vortical defects in the orientation field. The laning state is also observed at $\lambda = 0.1$ for low activity (Fig. 5.3 (b,d)). However, due to the weak anti-alignment, convective flows locally destabilize the global density lanes. Therefore, the lane structure rearranges continually over time.

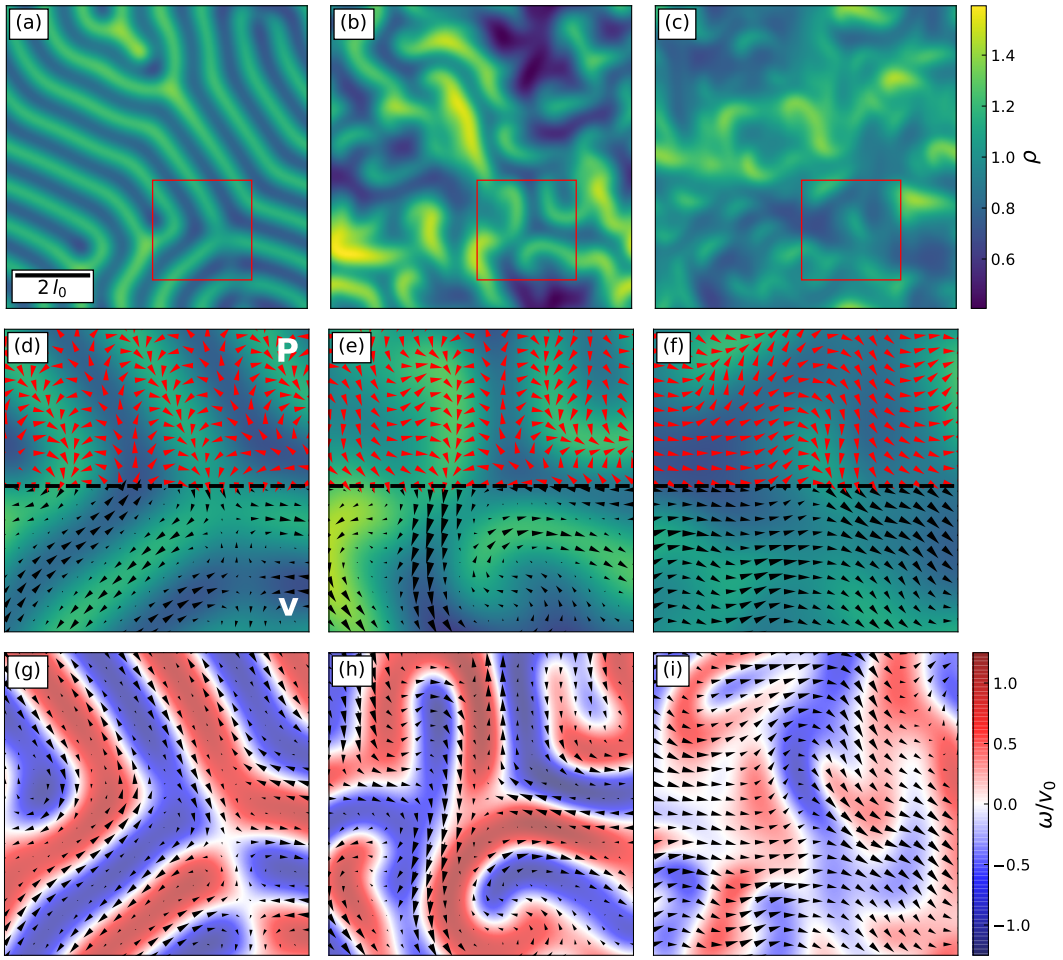

Fig. 5.4.: Snapshots of different states ordered by columns: left $\lambda = 0.6$ (laning), middle $\lambda = 0.1$ (turbulence), right $\lambda = 0.02$ (collective motion). (a-c) show the particle density over the hole simulation volume. The boxed region is magnified in (d-f) and (g-i) respectively. The second row shows the density, partially with the orientation field (red) and partially with the velocity field (black). The third row shows the velocity field and its vorticity $\omega = (\nabla \times \mathbf{v}) \cdot \hat{\mathbf{e}}_z$. A laning state with high and low density bands is found at intermediate anti-alignment strengths $\lambda = 0.6$. However, different to the overdamped limit system, no self-separation as in Fig. 5.2 is found since the necessary vortex defects in the orientation field are unstable due to advection. In the turbulent state, the laning structures become unstable resulting in strongly spatio-temporal fluctuations of the density. For the lowest observed λ, a global state of collective motion arises, slightly modulated by the anti-alignment and resulting density fluctuations. System parameters are $(m, v_0) = (0.1, 0.2)$ and $t = 5000$ for all systems.

Turbulence. Coming from the laning state in Fig. 5.3 (a,c) and lowering λ into the turbulent regime suddenly changes the dynamics considerably since now convective flows not only destabilize vortical defects in the orientation field but also the laning structures, due to the weakened anti-alignment. As can be seen from orientation field and vorticity in Fig. 5.4 (b,e,h), the laning structure evolves only locally. In this turbulent state, large fluctuations in the density field are observed. The system does no longer end in a steady state. Instead, the spatio-temporal fluctuations are self-sustained over time, explaining the large temporal variance of $\langle \Delta\rho \rangle$. The attached movies *TurbulenceOD.mp4* and *TurbulenceUD.mp4* , described in App. B, give an impression of the fluctuating density field. The non-steady character of the turbulent state results from the continues interplay of local lane formation and their destabilization due to convective flows, comparable to the instability of the previously discussed vortical defects in the laning state. The sudden increase of density fluctuations coincides with the onset of global velocity ordering in Fig. 5.3 (c). Since convective flows destabilize lane formation, the local alignment is no longer restricted to single lanes, resulting in a small but global drift velocity which is reflected in a moderate orientational order p_v. That inertial convection is indeed destabilizing the laning state is verified by switching off the convective terms in the dynamical equations of velocity and orientation within the underdamped PFC alignment model. Then local laning structures and vortical defects like in the overdamped model are observed, where otherwise turbulence would arise. When instead of λ the activity is lowered, the induced convective flows decrease also. For low enough v_0 again global laning structures emerge, corresponding to the transition in Fig. 5.3 (b,c).

Collective Motion. In the turbulent state anti-alignment is just weak enough so that laning is unstable, but still strong enough to inhibit global orientational order. This changes when λ is further lowered. Then, local alignment of orientations dominates over the weak anti-alignment, resulting in the emergence of global orientational order, see Fig. 5.3 (c). The homogeneous flow field transports particle density without accumulating it too much, leading to small density fluctuations comparable to the laning state or even smaller for the lowest λ. Since anti-alignment continually perturbs the homogeneous velocity field the temporal variance of $\langle \Delta\rho \rangle$ stays on a high level. As expected from these observations, the vorticity in the system is considerably lower compared to the laning or turbulent state. Example snapshots are given in Fig. 5.4 (c,f,i). It is suggested that convective flows stabilize the global collective motion, since they do not influence a homogeneous state of aligned orientations, but mix any arising misaligned

clusters with their surrounding due to advective transport of orientation. Therefore the formation of a larger alternatively orientated cluster is effectively inhibited.

Influence of Mass. It is striking that for both masses in Fig. 5.3 (b,d) the same results are found, although they differ by two orders of magnitude, which is expected to make the difference between over- and underdamped regime. The system is further investigated for mass dependent aspects by borrowing the concept of the spectral energy density $E_{\mathbf{k}}$ from classical turbulence theory. The aim of introducing this quantity is to gain insight into the length scales present in the velocity field, which might be influenced by mass dependent processes like damping. The spectral energy density is also used to characterize the phenomenom of active turbulence in overdamped incompressible systems [39, 47, 49, 58]. Following this approach, its common formal definition $\langle \mathbf{v}^2 \rangle = 2 \int d\mathbf{k}\ E_{\mathbf{k}}$ can also be stated as

$$E_{\mathbf{k}} := \frac{1}{2} \langle |\widetilde{v}_{\mathbf{k}}(t)|^2 \rangle \tag{5.10}$$

where $\widetilde{v}_{\mathbf{k}}$ is the Fourier component of the velocity field with wave vector $\mathbf{k}$. The scalar quantity E_k is obtained by summing $E_{\mathbf{k}}$ over spherical shells in Fourier space. It is used later on to quantify dominant length scales in the velocity field. It is noted that in principle a correct definition of spectral kinetic energy density would be to use the Fourier transform of $m\rho\mathbf{v}^2$ instead of $|\widetilde{\mathbf{v}}_{\mathbf{k}}|^2$ in the above definition, since the present system is compressible. Consequently, E_k should rather be interpreted as length scale resolved velocity statistics in the current context. However, the term spectral energy density is used further on for simplicity. In order to clarify the role of the different terms in the velocity equation for the spectral velocity statistics, a dynamical equation for $E_{\mathbf{k}}$ is formulated via the velocity equation in (5.6) which yields

$$\frac{dE_{\mathbf{k}}}{dt} = T_{conv} + T_{\gamma} + T_c + T_a \tag{5.11}$$

with the kinetic energy rates resulting from convection, damping, compressibility and activity, respectively. Those read

$$
\begin{aligned}
T_{conv} &= -\mathrm{Re}\left[\langle \widetilde{\mathbf{v}}_{\mathbf{k}}^{*} \cdot \mathfrak{F}\left[(\nabla \cdot \mathbf{v})\,\mathbf{v}\right]\rangle\right] \\
T_{\gamma} &= -\frac{2}{m}\, E_{\mathbf{k}} \\
T_{c} &= -\frac{1}{m}\mathrm{Re}\left[i\,\langle \widetilde{\mathbf{v}}_{\mathbf{k}}^{*} \cdot \mathbf{k}\,\widetilde{\rho}_{\mathbf{k}}\rangle\right] \\
T_{a} &= \frac{v_0}{m}\,\mathrm{Re}\left[\langle \widetilde{\mathbf{v}}_{\mathbf{k}}^{*} \cdot \widetilde{\mathbf{P}}_{\mathbf{k}}\rangle\right]
\end{aligned}
\tag{5.12}
$$

with the real part $\mathrm{Re}[\,\cdot\,]$ and complex conjugation *. Wherever a kinetic energy rate is positive it works as a source of velocity at that length scale and correspondingly for negative values as a sink. Although for under- and overdamped regime turbulence is observed in Fig. 5.3 (b,d) at high active drive, the corresponding energy rates in Fig. 5.5 differ. The shown values are averages over 300 time points in the range $t = 14000-20000$. For $m = 10$ the time derivative of E_k (sum over all rates) only slightly fluctuates around zero indicating that the time window used for averaging is large enough. However, the curve in the overdamped regime still systematically differs from zero. Therefore, those data should not be regarded as statistically significant but as a snapshot of a dynamics on longer time scales. Nevertheless, the fact that under- and overdamped regime differ here might lead to the physical conclusion that the long time statistics of density fluctuations depends on the mass parameter. However, whether this is correct, remains an open question in this work. In both mass regimes it is apparent that the strongly fluctuating T_c term corresponding to the compressibility of the system is the source of statistical uncertainty. It varies most since the density field can fluctuate on a global scale over time. Simulating larger systems might improve the statistical significance here.

Kinetic Energy Rates The curves for the other energy rates differ in the two mass regimes, indicating that the mechanism behind the observed turbulences also differ, respectively. The energy injection T_a due to activity and energy dissipation T_γ due to damping are one order of magnitude larger than the shown range and therefore only partially visible. Activity is the main source of kinetic energy, while damping is the main sink. Their effective contribution is shown as the difference $T_a - T_\gamma$. In the underdamped regime energy input from activity dominates at the preferred PFC wave number q_0, while dissipation is dominant at larger length scales, meaning smaller k values. Also the convective rate T_{conv} is relevant on those length scales, but with opposite sign. Physically this means that activity injects kinetic energy at q_0 which is then transported to larger

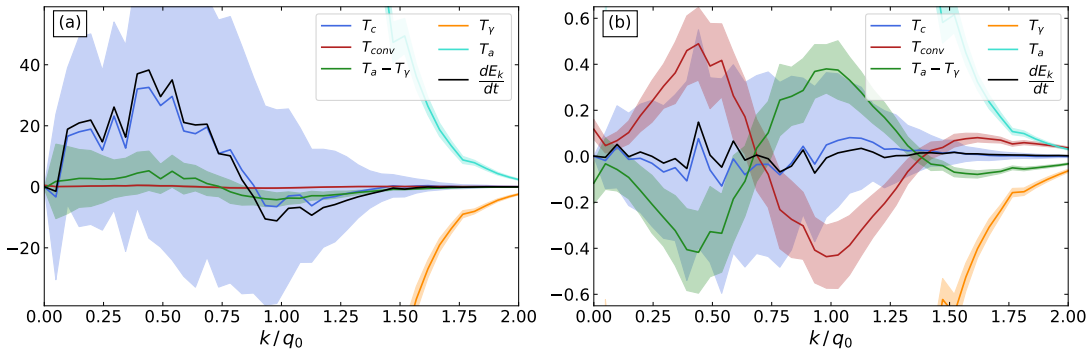

Fig. 5.5.: Kinetic energy rates in the over- and underdamped regime, (a) $m = 0.1$ and (b) $m = 10$, for systems in the active turbulence state $(v_0, \lambda) = (0.18, 0.1)$. The non-zero total energy rate in the overdamped regime shows that the averaged time span is too short to observe the statistically stationary state. As physically expected, convective transport of kinetic energy over different length scales is relatively low, however still necessary for the emergence of turbulence. Energy injection happens at length scales above q_0 ($T_a > T_\gamma$). It is unclear for now if this is characteristic for the emergence of turbulence in the overdamped regime or due to the too narrow averaged time span. In the underdamped regime, the balance of energy rates is composed differently. Activity injects kinetic energy into the system at the preferred scale q_0 ($T_a > T_\gamma$) which is then transported via convection to lower and partially also to higher wave numbers, where it is dissipated ($T_a < T_\gamma$).

length scales due to the high influence of convection and is finally dissipated there by the damping. Judging from the curves at higher k values this also happens in the direction of smaller length scales, but with lower rates. In the opposite overdamped regime the physics changes. The curve for T_{conv} has the same shape and amplitude as in the underdamped case. But now convection is only a small contribution compared to the influence of other terms. In the observed time frame the energy input from activity dominates the damping at length scales above l_0, which is different to the underdamped case. Whether this is an characteristic feature of the turbulence in the overdamped regime or just correlates with the also positive T_c term in this time frame remains unclear at this point since the time window for averaging is too short in the overdamped case to make statistical statements. It is noted that the convective contribution to the energy rate might be small in the overdamped regime, but is a necessary process for the emergence of the turbulent state. As explained earlier, the turbulent state (and collective motion) are absent when switching off the convective terms in the dynamical equations.

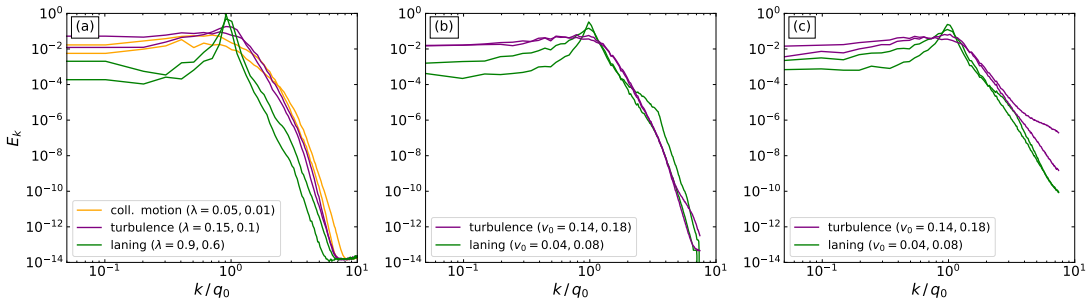

Fig. 5.6.: Distributions of energy spectra E_k. (a): Varying λ at fixed activity $v_0 = 0.2$ in the overdamped regime $m = 0.1$. While in the laning state velocities are sharply distributed at q_0, this peak broadens in the turbulent regime. In the collective motion state the dominant local alignment favours low wave numbers. (b): Varying v_0 for fixed anti-alignment $\lambda = 0.1$ in the overdamped regime $m = 0.1$. The broad velocity distribution in the turbulent state narrows again at q_0 when v_0 is lowered. Then, convective flows are too small to destabilize global density lanes completely. (c): Varying v_0 at fixed $\lambda = 0.1$, now in the underdamped regime $m = 10$. Slower decay of the velocity distribution above q_0 is observed, due to lower damping and convective transport of actively injected kinetic energy.

Spectral Energy Distributions. The dominant length scales in the velocity field change for the different observed states. This can be seen from the spectral energy distributions in Fig. 5.6. Possible mass influences are discussed later on. The curves in the turbulent regime $(v_0, \lambda) = (0.18, 0.1)$ for under- and overdamped mass parameter are time averaged as in Fig. 5.5. They vary the most, since here the highest spatio-temporal density fluctuations occur. All other curves are averaged over four time points in the interval $t = 14000 - 20000$.

In the laning state for high anti-alignment in Fig. 5.6 (a), velocity is predominantly accumulated at q_0, which is associated with the anti-parallel velocities in neighbouring density lanes. In the turbulent state the velocity distribution broadens to higher and lower length scales, since now anti-alignment is too weak to suppress convective flows. In the collective motion state, local alignment dominates anti-alignment resulting in a distribution where the peak at q_0 is strongly suppressed. Under- and overdamped spectral energies are compared in Fig. 5.6 (b,c). In both cases a high active drive v_0 causes turbulence with a broadened spectral energy distribution on cost of a narrow peak

at q_0. The increase of kinetic energy on higher length scales destabilizes density lanes at q_0 favoured by the anti-alignment. On the other hand, for small length scales, a difference between over- and underdamped systems arises. In the double logarithmic plot the curves show a power law dependence above q_0. Although the respective exponents differ they are not further discussed here quantitatively, since a improved numerical implementation and a higher maximum wavenumber is needed to extract reliable scaling exponents. Qualitatively, in the overdamped regime high wave numbers are strongly suppressed compared to the underdamped regime. One reason for this difference between the mass regimes is the increased damping for lower mass. Another reason might be the differing importance of convective flows for the distribution of kinetic energy over length scales, as discussed with the energy rates in Fig. 5.5. In the underdamped regime, activity injects kinetic energy into the system at q_0 which is then partially convected to smaller length scales, thereby increasing the tail of the velocity distribution there. This process is absent in the overdamped regime, where energy injection effectively happens at larger length scales and the damping rate even dominates above q_0, cpompare Fig. 5.5. However, as previously noted it remains unclear for now if the energy rates for $m = 0.1$ really reflect the characteristic process for the emergence of turbulence in the overdamped regime, since statistical uncertainties are present there.

Discussion

The found results in the underdamped PFC alignment model can be summarized as follows. For strong anti-alignment the system forms a global laning state of anti-parallel oriented high and low density bands. For lower λ and high active drive, convective flows induced by local alignment, destabilize this steady state, resulting in turbulence with high spatio-temporal density variations. The anti-alignment is still strong enough to inhibit global orientational order, which is then found in the low λ regime. Here, density fluctuations decrease again due to the homogeneous flow field.

Connection to Particle Model. The presented results can be directly connected to the ones in ref. [36], where a particle model with interactions comparable to the ones used here is investigated. The investigated model includes explicit particle short range alignment and anti-alignment at an higher length scale plus an repulsive interaction. The

hydrodynamic equations derived from this model are structurally similar to the overdamped limit of the PFC alignment model Eq. 5.1. Through particle simulations the authors identified a state transition from a periodic vortex lattice on the anti-alignment length scale to global orientational order by lowering the strength of the particle anti-alignment interaction. Instead of a global vortex lattice, the here presented model produces a laning state at high λ. This difference in results is explained with the different implementation of repulsion. In ref. [36] particles actively rotate their orientation to avoid high density regions, while in the present model this repulsion, modeled by the compressibility, is a passive one in the sense that it lowers a particle's velocity if it moves to higher densities instead of turning its orientation. But for the steady laning state, it is necessary that the region between lanes is balanced by a density gradient and oppositely pointing orientations. If particles would reorient at those gradients, the laning state becomes unstable. Because of this, a global vortex lattice is observed in ref. [36]. Although the motion is overdamped in this particle model, mesoscale turbulence is observed near the transition from the vortex to the ordered state which is explained with arising mesoscopic convective flows. This is in agreement with the fact that turbulence is found in the PFC alignment model only when the convective terms are included in the dynamical equations. It remains however unclear, how effective convection arises in the fully overdamped dynamics of the referenced particle model. It is suggested that the found laning state can also be produced in particle models similar to [36], however with a passive repulsive interaction and a lower compressibility as considered there.

Turbulence in Active Systems It is noted here that the turbulent state found in this work is conceptually different to what is commonly referred to as 'active turbulence' [39, 47, 58]. The latter denotes the phenomenon of turbulent-like states in completely overdamped and typically incompressible systems, like bacterial colonies. Such systems are often modeled via generalized Navier-Stokes equations for the velocity field where active stresses through hydrodynamic interactions are included with a term structurally equivalent to convection [39]. Therefore the turbulent patterns in such fully overdamped models can not arise from inertia, but from active interactions. Such interactions are not included in the PFC alignment model, where instead the convective terms responsible for the emergence of turbulence are a consequence of including inertia.

Suggestions for Future Work. Introducing finite mass and compressibility to the established minimal model for overdamped incompressible systems Eq. (2.27) shows some

interesting new aspects. Especially the found turbulent state needs further characterization, due to the above described differences from active turbulence states in incompressible systems. From the attached movies *TurbulenceOD.mp4* , *TurbulenceUD.mp4* it becomes apparent that the turbulent state within the PFC alignment model features local density fluctuations reminiscent to the global laning state. It is therefore suggested that the responsible flow field also shows such an anisotropy which could be a distinctive property of the turbulence in this compressible systems in which orientation and velocity field are treated seperatly and therefore can produce those laning like density fluctuations. This aspect can be investigated for example with spatially resolved velocity correlations, energy spectra or velocity increments [39, 58].
The kinetic energy rates and resulting spectra in Fig. 5.5 and Fig.5.6 already suggest that the mass parameter influences the dynamics in the turbulent state, since for higher masses the influence of convection on the velocity field dynamics increases. This might also lead to mass dependent time scales in the density fluctuations.

6. Conclusion

In this work two established models for overdamped active matter, the active phase field crystal model and a minimal model known in the context of active turbulence, are extended to the underdamped regime by explicitly including inertia. The general underdamped model which serves as a common basis for this, is derived from microscopic equations of motion.

It is shown within the underdamped active crystal model that the particle mass influences the collective relaxation dynamics to the traveling crystal state. Effective time scales for this process are extracted from a distinction of the transient dynamics into rotationally and translationally moving particle clusters. The non-trivial mass and activity dependence of these time scales is qualitatively explained with a mechanism for the formation and break-up of rotational clusters.

A comparison of the PFC alignment model with its overdamped counterpart reveals that inertially induced convective flows substantially influence the non-equilibrium state diagram. One noteworthy finding is the existence of a turbulent-like state in the underdamped model. As this state is self-sustained due to the interplay of active alignment and the therefore induced velocity field, it is different from classical turbulence in the sense that activity continually injects kinetic energy at an intermediate length scale. Also the found state conceptually differs from active turbulence in overdamped active systems, where spatio-temporal fluctuations are induced by additional active stresses in the system. Such active terms are not considered in the discussed PFC alignment model. Instead, the occurrence of the turbulent-like state (and the collective motion state) is traced back to the presence of solely inertial convection, which is absent in overdamped models.

The description of underdamped active systems through coarse-grained, hydrodynamic-like continuum models proved to be a useful approach to gain insight into the large scale collective dynamics. Some suggestions on how to proceed with the investigated systems are given in the respective discussions. A natural next step to extend the model proposed in Ch. 2.1, is to also include underdamped rotational motion of particles with a moment of inertia I. A starting point for the derivation of a corresponding continuum model in two dimensions are microscopic equations of motion of the form

$$
\begin{aligned}
\frac{\mathrm{d}\mathbf{r}_i}{\mathrm{d}t} &= \frac{\mathbf{p}_i}{m} \\
\frac{\mathrm{d}\mathbf{p}_i}{\mathrm{d}t} &= -\gamma\,\mathbf{p}_i + \mathbf{F}_i(\mathbf{r}^N) + f_0\,\hat{\mathbf{u}}_i + \sqrt{2D}\;\boldsymbol{\Gamma}_i(t) \\
\frac{\mathrm{d}\varphi_i}{\mathrm{d}t} &= \omega_i \\
I\,\frac{\mathrm{d}\omega_i}{\mathrm{d}t} &= -\alpha_R\,\omega_i + G_i(\mathbf{r}^N, \varphi^N) + \sqrt{2D_R}\;\xi_i(t)
\end{aligned}
\tag{6.1}
$$

with the angular velocity ω_i for each particle. For single active particles it is already shown that a finite angular moment of inertia influences even the long time dynamics [11]. An interplay of inertial rotational motion and alignment mechanisms might open the door to additional possibilities of controlling the collective behaviour in active matter.

Literature

[1] J. Deseigne, S. Léonard, O. Dauchot, and H. Chaté, "Vibrated polar disks: Spontaneous motion, binary collisions, and collective dynamics", *Soft Matter*, vol. 8, no. 20, pp. 5629–5639, 2012.

[2] M. C. Marchetti, J.-F. Joanny, S. Ramaswamy, T. B. Liverpool, J. Prost, M. Rao, and R. A. Simha, "Hydrodynamics of soft active matter", *Reviews of Modern Physics*, vol. 85, no. 3, p. 1143, 2013.

[3] C. Bechinger, R. Di Leonardo, H. Löwen, C. Reichhardt, G. Volpe, and G. Volpe, "Active particles in complex and crowded environments", *Reviews of Modern Physics*, vol. 88, no. 4, p. 045 006, 2016.

[4] A. Doostmohammadi, J. Ignés-Mullol, J. M. Yeomans, and F. Sagués, "Active nematics", *Nature communications*, vol. 9, no. 1, p. 3246, 2018.

[5] A. M. Menzel, "Tuned, driven, and active soft matter", *Physics reports*, vol. 554, pp. 1–45, 2015.

[6] P. Romanczuk, M. Bär, W. Ebeling, B. Lindner, and L. Schimansky-Geier, "Active brownian particles-from individual to collective stochastic dynamics p.", *The European Physical Journal Special Topics*, vol. 202, 2012.

[7] L. Giomi, "Geometry and topology of turbulence in active nematics", *Physical Review X*, vol. 5, no. 3, p. 031 003, 2015.

[8] J. Palacci, S. Sacanna, A. P. Steinberg, D. J. Pine, and P. M. Chaikin, "Living crystals of light-activated colloidal surfers", *Science*, vol. 339, no. 6122, pp. 936–940, 2013.

[9] D. P. Zitterbart, B. Wienecke, J. P. Butler, and B. Fabry, "Coordinated movements prevent jamming in an emperor penguin huddle", *PLoS one*, vol. 6, no. 6, e20260, 2011.

[10] H. Risken, "Fokker-planck equation", in *The Fokker-Planck Equation*, Springer, 1996, pp. 63–95.

[11] C. Scholz, S. Jahanshahi, A. Ldov, and H. Löwen, "Inertial delay of self-propelled particles", *Nature communications*, vol. 9, no. 1, p. 5156, 2018.

[12] M. C. Cross and P. C. Hohenberg, "Pattern formation outside of equilibrium", *Reviews of modern physics*, vol. 65, no. 3, p. 851, 1993.

[13] H. Emmerich, H. Löwen, R. Wittkowski, T. Gruhn, G. I. Tóth, G. Tegze, and L. Gránásy, "Phase-field-crystal models for condensed matter dynamics on atomic length and diffusive time scales: An overview", *Advances in Physics*, vol. 61, no. 6, pp. 665–743, 2012.

[14] K. Elder, M. Katakowski, M. Haataja, and M. Grant, "Modeling elasticity in crystal growth", *Physical review letters*, vol. 88, no. 24, p. 245 701, 2002.

[15] K. Elder and M. Grant, "Modeling elastic and plastic deformations in nonequilibrium processing using phase field crystals", *Physical Review E*, vol. 70, no. 5, p. 051 605, 2004.

[16] K. R. Elder, N. Provatas, J. Berry, P. Stefanovic, and M. Grant, "Phase-field crystal modeling and classical density functional theory of freezing", *Physical Review B*, vol. 75, no. 6, p. 064 107, 2007.

[17] J. Swift and P. C. Hohenberg, "Hydrodynamic fluctuations at the convective instability", *Physical Review A*, vol. 15, no. 1, p. 319, 1977.

[18] S. van Teeffelen, R. Backofen, A. Voigt, and H. Löwen, "Derivation of the phase-field-crystal model for colloidal solidification", *Physical Review E*, vol. 79, no. 5, p. 051 404, 2009.

[19] A. M. Menzel and H. Löwen, "Traveling and resting crystals in active systems", *Physical review letters*, vol. 110, no. 5, p. 055 702, 2013.

[20] A. M. Menzel, T. Ohta, and H. Löwen, "Active crystals and their stability", *Physical Review E*, vol. 89, no. 2, p. 022 301, 2014.

[21] M. Rex, H. Wensink, and H. Löwen, "Dynamical density functional theory for anisotropic colloidal particles", *Physical Review E*, vol. 76, no. 2, p. 021 403, 2007.

[22] J. Toner and Y. Tu, "Flocks, herds, and schools: A quantitative theory of flocking", *Physical review E*, vol. 58, no. 4, p. 4828, 1998.

[23] L. Ophaus, S. V. Gurevich, and U. Thiele, "Resting and traveling localized states in an active phase-field-crystal model", *Physical Review E*, vol. 98, no. 2, p. 022 608, 2018.

[24] Y. Sumino, K. H. Nagai, Y. Shitaka, D. Tanaka, K. Yoshikawa, H. Chaté, and K. Oiwa, "Large-scale vortex lattice emerging from collectively moving microtubules", *Nature*, vol. 483, no. 7390, p. 448, 2012.

[25] C. Dombrowski, L. Cisneros, S. Chatkaew, R. E. Goldstein, and J. O. Kessler, "Self-concentration and large-scale coherence in bacterial dynamics", *Physical review letters*, vol. 93, no. 9, p. 098 103, 2004.

[26] I. H. Riedel, K. Kruse, and J. Howard, "A self-organized vortex array of hydrodynamically entrained sperm cells", *Science*, vol. 309, no. 5732, pp. 300–303, 2005.

[27] N. S. Rossen, J. M. Tarp, J. Mathiesen, M. H. Jensen, and L. B. Oddershede, "Long-range ordered vorticity patterns in living tissue induced by cell division", *Nature communications*, vol. 5, p. 5720, 2014.

[28] H. Reinken, S. H. Klapp, M. Bär, and S. Heidenreich, "Derivation of a hydrodynamic theory for mesoscale dynamics in microswimmer suspensions", *Physical Review E*, vol. 97, no. 2, p. 022 613, 2018.

[29] S. Heidenreich, J. Dunkel, S. H. Klapp, and M. Bär, "Hydrodynamic length-scale selection in microswimmer suspensions", *Physical Review E*, vol. 94, no. 2, p. 020 601, 2016.

[30] A. M. Menzel, A. Saha, C. Hoell, and H. Löwen, "Dynamical density functional theory for microswimmers", *The Journal of chemical physics*, vol. 144, no. 2, p. 024 115, 2016.

[31] M. Ballerini, N. Cabibbo, R. Candelier, A. Cavagna, E. Cisbani, I. Giardina, V. Lecomte, A. Orlandi, G. Parisi, A. Procaccini, *et al.*, "Interaction ruling animal collective behavior depends on topological rather than metric distance: Evidence from a field study", *Proceedings of the national academy of sciences*, vol. 105, no. 4, pp. 1232–1237, 2008.

[32] F. Ginelli and H. Chaté, "Relevance of metric-free interactions in flocking phenomena", *Physical Review Letters*, vol. 105, no. 16, p. 168 103, 2010.

[33] A. Kudrolli, G. Lumay, D. Volfson, and L. S. Tsimring, "Swarming and swirling in self-propelled polar granular rods", *Physical review letters*, vol. 100, no. 5, p. 058 001, 2008.

[34] A. Bricard, J.-B. Caussin, D. Das, C. Savoie, V. Chikkadi, K. Shitara, O. Chepizhko, F. Peruani, D. Saintillan, and D. Bartolo, "Emergent vortices in populations of colloidal rollers", *Nature communications*, vol. 6, p. 7470, 2015.

[35] A. M. Menzel, "Unidirectional laning and migrating cluster crystals in confined self-propelled particle systems", *Journal of Physics: Condensed Matter*, vol. 25, no. 50, p. 505 103, 2013.

[36] R. Großmann, P. Romanczuk, M. Bär, and L. Schimansky-Geier, "Vortex arrays and mesoscale turbulence of self-propelled particles", *Physical review letters*, vol. 113, no. 25, p. 258 104, 2014.

[37] H. Wensink and H. Löwen, "Emergent states in dense systems of active rods: From swarming to turbulence", *Journal of Physics: Condensed Matter*, vol. 24, no. 46, p. 464 130, 2012.

[38] S. R. McCandlish, A. Baskaran, and M. F. Hagan, "Spontaneous segregation of self-propelled particles with different motilities", *Soft Matter*, vol. 8, no. 8, pp. 2527–2534, 2012.

[39] H. H. Wensink, J. Dunkel, S. Heidenreich, K. Drescher, R. E. Goldstein, H. Löwen, and J. M. Yeomans, "Meso-scale turbulence in living fluids", *Proceedings of the National Academy of Sciences*, vol. 109, no. 36, pp. 14 308–14 313, 2012.

[40] G. Ariel, M. Sidortsov, S. D. Ryan, S. Heidenreich, M. Bär, and A. Be'er, "Collective dynamics of two-dimensional swimming bacteria: Experiments and models", *Physical Review E*, vol. 98, no. 3, p. 032 415, 2018.

[41] S. Chandragiri, A. Doostmohammadi, J. M. Yeomans, and S. P. Thampi, "Active transport in a channel: Stabilisation by flow or thermodynamics", *Soft matter*, vol. 15, no. 7, pp. 1597–1604, 2019.

[42] R. Mueller, J. M. Yeomans, and A. Doostmohammadi, "Emergence of active nematic behavior in monolayers of isotropic cells", *Physical review letters*, vol. 122, no. 4, p. 048 004, 2019.

[43] A. J. Archer, "Dynamical density functional theory for molecular and colloidal fluids: A microscopic approach to fluid mechanics", *The Journal of chemical physics*, vol. 130, no. 1, p. 014 509, 2009.

[44] U. M. B. Marconi and P. Tarazona, "Dynamic density functional theory of fluids", *The Journal of chemical physics*, vol. 110, no. 16, pp. 8032–8044, 1999.

[45] J.-P. Hansen and I. R. McDonald, *Theory of simple liquids*. Elsevier, 1990.

[46] F. C. Frank, "I. liquid crystals. on the theory of liquid crystals", *Discussions of the Faraday Society*, vol. 25, pp. 19–28, 1958.

[47] V. Bratanov, F. Jenko, and E. Frey, "New class of turbulence in active fluids", *Proceedings of the National Academy of Sciences*, vol. 112, no. 49, pp. 15 048–15 053, 2015.

[48] J. Dunkel, S. Heidenreich, M. Bär, and R. E. Goldstein, "Minimal continuum theories of structure formation in dense active fluids", *New Journal of Physics*, vol. 15, no. 4, p. 045 016, 2013.

[49] M. James, W. J. Bos, and M. Wilczek, "Turbulence and turbulent pattern formation in a minimal model for active fluids", *Physical Review Fluids*, vol. 3, no. 6, p. 061 101, 2018.

[50] M. Frigo and S. Johnson, "FFTW: An adaptive software architecture for the FFT", in *Proc. 1998 IEEE Intl. Conf. Acoustics Speech and Signal Processing*, vol. 3, IEEE, 1998, pp. 1381–1384.

[51] D. Gottlieb and S. A. Orszag, *Numerical analysis of spectral methods: Theory and applications*. Siam, 1977, vol. 26.

[52] R. C. Swanson and E. Turkel, "On central-difference and upwind schemes", *Journal of computational physics*, vol. 101, no. 2, pp. 292–306, 1992.

[53] D. Grossman, I. S. Aranson, and E. B. Jacob, "Emergence of agent swarm migration and vortex formation through inelastic collisions", *New Journal of Physics*, vol. 10, p. 023 036, 2008.

[54] S. Praetorius, A. Voigt, R. Wittkowski, and H. Löwen, "Active crystals on a sphere", *Physical Review E*, vol. 97, no. 5, p. 052 615, 2018.

[55] M. E. Cates and J. Tailleur, "Motility-induced phase separation", *Annu. Rev. Condens. Matter Phys.*, vol. 6, no. 1, pp. 219–244, 2015.

[56] S. Mandal, B. Liebchen, and H. Löwen, "Motility-induced temperature difference in coexisting phases", *arXiv preprint arXiv:1902.06116*, 2019.

[57] M. Abkenar, K. Marx, T. Auth, and G. Gompper, "Collective behavior of penetrable self-propelled rods in two dimensions", *Physical Review E*, vol. 88, no. 6, p. 062 314, 2013.

[58] M. James and M. Wilczek, "Vortex dynamics and lagrangian statistics in a model for active turbulence", *The European Physical Journal E*, vol. 41, no. 2, p. 21, 2018.

Appendices

A. Linear Stability Analysis

Here the predicted shift of the phase diagram Eq. (4.2) is derived via linear stability analysis of the resting crystalline state.
In the steady state the velocity field is stationary in time. Therefore the same quasi stationary approximation as in the overdamped limit Eqs. (2.26) can be made. Then the underdamped model Eqs. (2.22) simplify to

$$\begin{aligned}\frac{\partial \rho}{\partial t} &= \frac{|\overline{\rho}|}{\gamma m}\nabla^2\left[\epsilon + \lambda\left(q_0^2+\nabla^2\right)^2 + u\,\rho^2\right]\rho - |\overline{\rho}|\,v_0\,\nabla\cdot\mathbf{P}\\ \frac{\partial \mathbf{P}}{\partial t} &= \left(C_1\,\nabla^2 - D_R\right)\mathbf{P} - \frac{v_0}{|\overline{\rho}|}\,\nabla\rho.\end{aligned} \tag{A.1}$$

This linear system of equations for ρ and $\mathbf{P}$ can be solved by the solutions ρ_0 and $\mathbf{P_0}$ found in the steady state of the simulations. Next, Eqs. (A.1) are linearized with respect to small perturbations $\delta\rho$ and $\delta\mathbf{P}$ of the fields

$$\rho = \rho_0(\mathbf{r}) + \delta\rho(\mathbf{r},t), \qquad \mathbf{P} = \mathbf{P_0}(\mathbf{r}) + \delta\mathbf{P}(\mathbf{r},t) \tag{A.2}$$

which reads

$$\partial_t \begin{pmatrix}\delta\rho\\ \delta P_x\\ \delta P_y\end{pmatrix} = \begin{pmatrix}\frac{|\overline{\rho}|}{\gamma m}\nabla^2\left[\omega(\nabla^2)+3u\rho_0\right] & -|\overline{\rho}|\,v_0\partial_x & -|\overline{\rho}|\,v_0\partial_y\\ -\frac{v_0}{|\overline{\rho}|}\partial_x & (C_1\nabla^2 - D_R) & 0\\ -\frac{v_0}{|\overline{\rho}|}\partial_y & 0 & (C_1\nabla^2 - D_R)\end{pmatrix}\begin{pmatrix}\delta\rho\\ \delta P_x\\ \delta P_y\end{pmatrix} \tag{A.3}$$

with the PFC part $\omega(\nabla^2) = \epsilon + \lambda\left(q_0^2+\nabla^2\right)^2$. Of special interest is the stability of the PFC length scale q_0. Therefore and for simplicity the perturbations are chosen to be

$$\delta\rho = e^{\sigma t}a_{n,m}\sum_{n,m} e^{i\mathbf{G}_{n,m}\mathbf{r}}, \qquad \delta\mathbf{P} = -\mathbf{b}_{n,m}\nabla\delta\rho \tag{A.4}$$

with amplitudes $a_{n,m}$ and $\mathbf{b}_{n,m}$. The triangular reciprocal lattice vector $\mathbf{G}_{n,m} = n\mathbf{g_1} + m\mathbf{g_2}$ is a superposition of the primitive lattice vectors $\mathbf{g_1}$, $\mathbf{g_2}$. (n, m) can be all pairs of integer numbers with $G_{n,m}^2 = q_0^2$. Inserting these perturbations into Eq. (A.3) and taking the fourier transformation results in an eigenvalue problem for the amplitudes of each mode

$$(M - \sigma \mathbb{1}) \begin{pmatrix} a_{n,m} \\ b_{n,m\ x} \\ b_{n,m\ y} \end{pmatrix} = 0 \tag{A.5}$$

with the matrix

$$M = \begin{pmatrix} -\frac{|\overline{\rho}|q_0^2}{\gamma m}\left[\epsilon + 3u\, C(\rho_0^2)\right] & |\overline{\rho}|\, v_0\, G_{n,m\,x}^2 & |\overline{\rho}|\, v_0\, G_{n,m\,y}^2 \\ -\frac{v_0}{|\overline{\rho}|} i\, G_{n,m\,x} & -\left(C_1 q_0^2 + D_R\right) i G_{n,m\,x} & 0 \\ -\frac{v_0}{|\overline{\rho}|} i\, G_{n,m\,y} & 0 & -\left(C_1 q_0^2 + D_R\right) i G_{n,m\,y} \end{pmatrix}. \tag{A.6}$$

Here the convolution in fourier space $C(\rho_0^2) = \mathfrak{F}[\rho_0^2] * \left(\sum_{n,m} \delta\left(\mathbf{k} - \mathbf{G}_{n,m}\right)\right)$ is used for clear notation and $\omega(-q_0^2) = \epsilon$. The absence of non-negative eigenvalues σ is the criterion for the linear stability of the hexagonal phase. All possible eigenvalues are solutions of the characteristic equation

$$\det\left(M - \sigma \mathbb{1}\right) = -\sigma^3 + b\sigma^2 + c\sigma + d = 0 \tag{A.7}$$

with coefficients b, c, d. From this it can be seen that a necessary condition for solely negative eigenvalues is $d < 0$. Explicitly this reads

$$\begin{aligned} & d = M_{11}M_{22}M_{33} - M_{11}M_{32}M_{23} - M_{33}M_{21}M_{12} - M_{31}M_{22}M_{13} < 0 \\ \Leftrightarrow\ & \epsilon < -\frac{v_0^2 \gamma m}{\left(C_1 q_0^2 - D_R\right)|\overline{\rho}|} \frac{G_{n,m\,x} + G_{n,m\,y}}{G_{n,m\,x} G_{n,m\,y}} - 3u\, C(\rho^2) \end{aligned} \tag{A.8}$$

which is the result for the shift of the phase boundary

$$\Delta\epsilon \propto \frac{v_0^2 \gamma m}{C_1 q_0^2 - D_R} \tag{A.9}$$

also found by Menzel *et al.* where the rotational diffusion needs to be re-parametrized as $D_R \to D_R C_1$ to coincide with [19]. Note that here occurs the additional dependence on $\alpha = \gamma m$.

B. Description of Attached Videos

ActiveCrystal.mp4

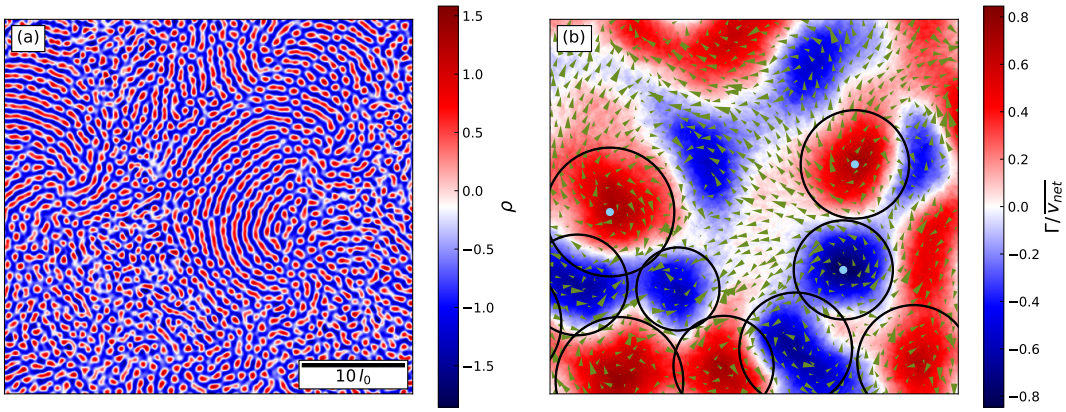

Fig. B.1.: (a): Density field for the first frame of the attached movie *ActiveCrystal.mp4*. (b): Circulation field and particle velocities. At this intermediate time particles are aligned locally and have build rotating clusters. The ones whose centers are marked with a dot are best visible by eye. Particles leaving the cluster radially outward are replaced by incoming ones from surrounding clusters of translational moving groups. The system parameters read $(m, v_0) = (2, 0.4)$ and $t = 500$.

ActiveCrystalAdvection.mp4

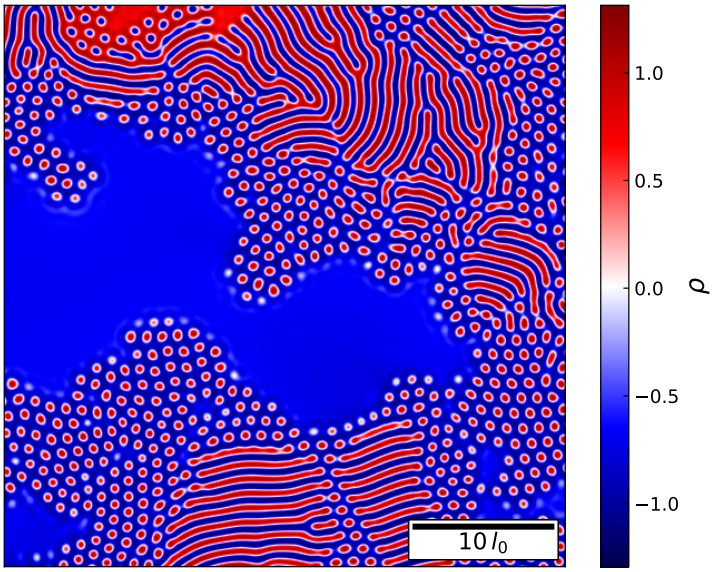

Fig. B.2.: Density field for the first frame of the attached movie *ActiveCrystalAdvection.mp4*. Density, transported by the crystalline regions, accumulates over time to a constant high density cluster. The system parameters read $(m, v_0) = (0.1, 0.4)$ and $t = 750$.

TurbulenceOD.mp4 , *TurbulenceUD.mp4*

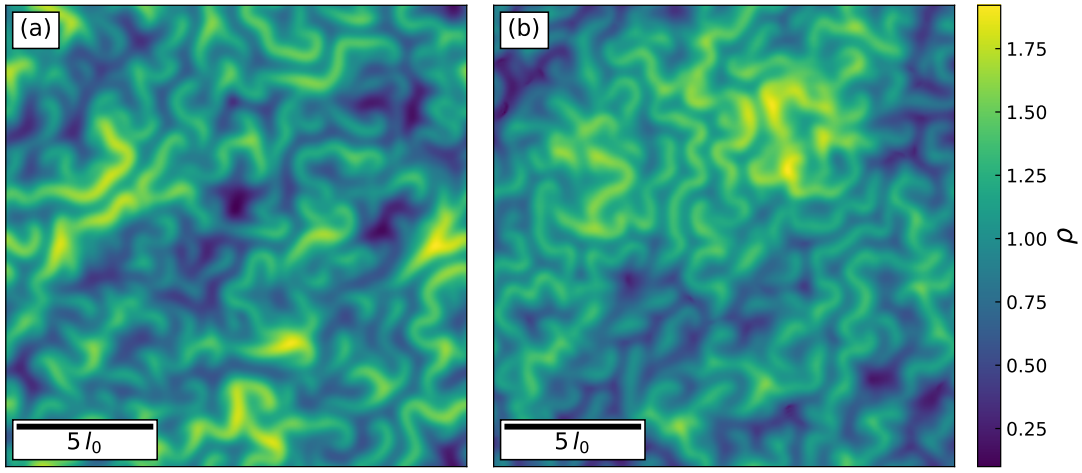

Fig. B.3.: Density field for the first frame of the attached movies (a) *TurbulenceOD.mp4* ($m = 0.1$) and *TurbulenceUD.mp4* ($m = 10$). In this turbulence state, locally arising laning structures in the density field are continually destabilized by convective flows. $\lambda = 0.1$ and $t = 750$.